Universidad de Sonora

Departamento de Investigación en Física

Posgrado en Ciencias (Física)

# INFRARED THERMOGRAPHY STUDIES ON THE PHOTOTHERMAL EFFECT OF GOLD NANOPARTICLES IN WATER

Submitted in partial fulfillment of the requirements for the degree of

**Master of Science in Physics**

By:

**Jose Luis Ibarra Valdez**

**B.Sc (Physics)**

Hermosillo, Sonora, 2018

# Universidad de Sonora

Repositorio Institucional UNISON


"El saber de mis hijos hará mi grandeza"


Excepto si se señala otra cosa, la licencia del ítem se describe como openAccess

**The studies realized in this work were approved by the Sociedad Mexicana de Física to appear in the LIX CONGRESO NACIONAL DE FÍSICA with the title "632 nm laser heating of gold nanoparticles in water: experiment and computer simulations" with the registration number 1079.**

## Dedication

To Adriana; My family and friends.

## Acknowledgements

Firstly, I would like to express my sincere gratitude to my advisor Dr. Valery Chernov for the continuous support of my study and related research, for his patience, motivation, and immense knowledge. His guidance helped me in all the time of research and writing of this thesis. And for giving me the opportunity to work alongside. Besides my advisor, I would like to thank the rest of my thesis committee: Dr. Marcelino Barboza and Dr. Martín Pedroza, for their insightful comments and encouragement, but also for the hard question which incented me to widen my research from various perspectives. Last but not the least, I would like to thank CONACyT for giving me the opportunity to continue studying

**Abstract**

Infrared (IR) thermography has been utilized in the last decades for the detection of many diseases. With the growth of nanotechnology as also grown the investigation of the interactions between electromagnetic radiation and metallic nanoparticles and its heat transfer property. Such property is often used in medicine as a hyperthermia treatment for cancer.

Due the importance of the heated nanoparticle applications it is a need to have a system that can monitor, recollect, process, and analyze data information coming from heated bodies. Being so, the general objective of this work is the development of an IR thermography based method to study thermal effects on surfaces.

This works presents a new improved method of monitoring surface temperature changes by dynamic IR thermography. The method is based on the careful analysis of IR image sequences that allows one to select areas with significant temperature variation and evaluate temporal behavior of the surface temperature. A set of codes was written in MATLAB software to analyze the superficial changes in temperature for systems that present a volumetric or superficial heating process.

To test the method, the experimental study on the photothermal effect in a gold hydrosol containing 0.3 mg/mL hollow GNPs was performed. A simple set up was designed to heat the hydrosol by laser light and monitor the hydrosol surface temperature by IR camera. It was shown that the surface temperature under the laser beam gradually increases and reaches a saturation level. The surface temperature distribution exhibit the concentric structure with the maximal temperature in the beam center. After the laser was turned off, the temperature returned to equilibrium with the area outside of the beam in about ten seconds.

Numerical simulations of the experiment with the COMSOL Multiphysics Heat Transfer module were used to reproduce the measured surface temperatures and estimate the heat transfer coefficient at the hydrosol surface and photothermal conversion efficiency, the parameters that would be difficult to find byother methods.

In conclusion, this work presents a new improved method for the data acquisition and data analysis based on dynamic IR thermography. This method is not limited to colloids with nanoparticles, but it can be applied for any system whose superficial temperature is change under an external stimulation. Despite the IR thermography measures only a surface temperature, it is

possible, combining the precise surface temperature detection and results of numerical simulations with an adequate model, to estimate the volumetric temperature and determine 3D heat delivery during the hyperthermia procedure.

## CONTENT

## Abbreviations

| Abbreviation | Meaning |
|---|---|
| • CW | • Continuous wave |
| • GNP | • Gold Nanoparticle |
| • IR | • Infrared |
| • MRI | • Magnetic resonance imaging |
| • NP | • Nanoparticle |
| • RTD | • Radial temperature distribution |
| • SAR | • Specific absorption rate |
| • SD | • Standard deviation |

## Thesis Outline

The thesis consists of four chapters related to IR thermography, some of its applications and the development of a system for the analysis of thermal information from IR cameras. Such analysis consists on finding a temperature distribution for the surface of the system and give a phenomenological description of it. Also, numerical simulations are made to found parameters that would be difficult to determine by other ways.

The second chapter contains a literature review on the photothermal effect of metal plasmonic nanoparticles in water under light illumination. The heat generation in plasmonic NPs under light illumination is also discussed. Then, the temperature distribution in a media with heating nanoparticles at macro-, micro-, and nano-scale levels will be considered. The final part of this chapter is devoted to the overview of experimental measurements of the light-to heat conversion in metal hydrosols.

A novel IR thermography method of study on the photothermal effect in plasmonic nanoparticles immersed in dielectric media illuminated with light is presented in chapter three. As a model system was chosen a water colloid of GNPs (gold hydrosol) under continuous wave illumination with laser. Description of the experimental measurement of the light-to-heat

conversion by the IR thermography methods. Pre-processing of IR images and evaluation of the temperature distributions in the near-surface layer are presented

In chapter 4, a theoretical analysis of the radial temperature distributions in the gold hydrosol under illumination with a laser light are presented. The analysis is based on the numerical calculations performed with the finite-elements software COMSOL Multiphysics.

# CHAPTER I: INTRODUCTION

## 1.1 Background

IR thermography has been used since the past decades in the detection of many diseases. Usually, an abnormal change in body temperature can be related to a sickness. With the recent advances in the field of nanotechnology, the effects of interaction between laser and noble metal nanoparticles have been increased. Such interactions include principally thermic effects that can be used to enhance some treatments. The study of photo thermal effects on metal nanoparticles is very important because of its application in the field of medicine. There are nowadays plenty of studies of thermal responses of plasmonic nanoparticles when stimulated with light.

## 1.2 Motivation and objectives

Infrared (IR) thermography has been utilized in the last decades for the detection of many diseases. With the growth of nanotechnology as also grown the investigation of the interactions between electromagnetic radiation and metallic nanoparticles and its heat transfer property. Such property is often used in medicine as a hyperthermia treatment for cancer.

Due the importance of the heated nanoparticle applications it is a need to have a system that can monitor, recollect, process, and analyze data information coming from heated bodies. Being so, the general objective of the thesis is the development of an improved method of monitoring surface temperature changes by dynamic IR thermography caused by surface or volumetric heating processes due to the external stimulation. The following partial objectives have been established in order to achieve the general objective.

To design a simple experimental set up for illumination a surface under study by laser light and monitoring the surface temperature by IR camera.

To perform the experimental study on the photothermal effect in a gold hydrosol containing 0.3 mg/mL hollow GNPs and to obtain a set of raw IR images of the laser illuminated surface.

To develop a method for careful analysis of IR image sequences, which allows one to select areas with significant temperature variation and evaluate temporal behavior of the surface temperature.

To write a set of codes in MATLAB software realizing the developed method.

To apply the developed method to the obtain set of raw IR images and evaluate spatiotemporal behavior the surface temperature during and after laser illumination.

To build COMSOL model for simulation photothermal effect in illuminated gold hydrosol with COMSOL Multiphysics Heat Transfer module.

To perform numerical simulations of the experiment with the COMSOL aiming to reproduce the measured surface temperatures.

To compare both, experimental and computational results and estimate the heat transfer coefficient at the hydrosol surface and photothermal conversion efficiency, the parameters that might be difficult to determine with other methods.

# CHAPTER 2

# LIGHT INDUCED HEATING IN A MEDIA WITH EMBEDDED METAL NANOPARTICLES (LITERATURE SURVEY)

This chapter contains a literature review on the photothermal effect of metal plasmonic nanoparticles in water under light illumination. There are several names for the heterogeneous mixture of gold nanoparticle and water. The most used of them are the solution or suspension of GNPs in water. To our opinion, both name are incorrect: the term solution means that the size of the dissolved phase is less than 1 nanometer while for the suspension the size of the dissolved phase is more than 1 micron [http://www.chemistrylearning.com/colloidal-solution-true-solution-and-suspension/]. The appropriate name for the dispersion with the dispersed phase, which size is between 1 nanometer and 1 micrometer is colloid [http://goldbook.iupac.org/html/C/C01172.html]. The specific name for colloid with the solid continuous phase is sol. Therefore, the correct name for the mixture of metal NPs in water is metal hydrosol and, more specifically, gold hydrosol when nanoparticles are made of gold.

In the first subsection, the heat generation in plasmonic NPs under light illumination is discussed. Then, the temperature distribution in a media with heating nanoparticles at macro-, micro- and nano-scale levels will be considered. The third subchapter is devoted to the overview of experimental measurements of the light-to heat conversion in metal hydrosols.

## 2.1 Light-to Heat Conversion by Plasmonic Nanoparticles

The efficiency of light-to heat conversion by an individual NP is determined by the shape and size of NPs, the wavelength and pulse duration the illuminating light and the thermal properties of NPs and a surrounding medium. efficiency of light-to-heat conversion is also discussed. Below we will consider the optical properties of plasmonic NPs embedded in a dielectric medium and the heat generation in a NP illuminated with light.

### 2.1.1 Optical Properties of Metal Nanoparticles

When a nanoparticle immersed in a host medium is illuminated, part of the intercepted light is scattered in the surroundings while the other part is absorbed and ultimately dissipated into

heat (Janie et al., 2006). The efficiency of each of these processes is characterized by $\sigma_s$ and $\sigma_a$, the elastic scattering and the absorption cross-sections, respectively. The sum of these two processes leads to light attenuation characterized by the extinction cross-section $\sigma_{ex}$:

$$\sigma_{ex} = \sigma_s + \sigma_a \qquad (2.1.1)$$

Depending on the size and the shape of the nanoparticle, the balance between scattering and absorption can vary substantially. For instance, while small gold spheres (<10 nm in diameter) mainly act as invisible Nano sources of heat, scattering processes dominate for diameters larger than ~50 nm ], Jain et al., (2006).

Here, we focus on the absorption processes and the subsequent heat generation. The heat generation of single NPs is correlated with macroscopic measurable SAR. With the heat generated by NPs, the nanoscale, microscale, and macroscale thermal responses are analyzed within the continuum regime.

It is known that metallic NP in the absorption and scattering spectra show resonance in the UV-Vis region. Bands that does not appear in a macroscopic level. These bands are related to the conduction electrons' behavior when interacting with light waves.

Free electrons in the material can travel freely through the metal. When a wavelength from a light source is larger than the particle size it can make, conditions leading to resonance. This light causes the free electrons to oscillate within the metal. The resonance condition is found with absorption and scattering spectroscopy and it is found to depend on material and surrounding medium size, dielectric constant. If the geometry of NP changes, also change the oscillation frequency of electrons, generating different cross sections due to light interaction.

A plasmon is a collective oscillation of electrons in a material. Plasmon is the same phenomenon as a SPR but plasmons are constrained by the colloid of NP. To induce a plasmon in a colloid takes much less effort than in a continuous film because there is no need for special conditions. Incident light interacts directly with the colloid and its surroundings.

A numer of papers are devoted to the study on the optical properties of NP colloids ,Eustis, et al., (2006); Khlebstov et al., (2008); Lakiwicz et al., (2006); Suichi et al.,(2012) , the most common theory to describe them is the Mie theory. This is a relatively simple theory applied to spherical NP. The cross section for extinctions is given by

$$\sigma_{ext} = \sigma_s + \sigma_a = k_1 \,\mathrm{Im}(\alpha) + \frac{k_1^4}{6\pi} |\alpha|^2 \qquad (2.1.2)$$

where $k_1 = \frac{2\pi n_1}{\lambda_0}$ is the wave vector of the incident light in medium 1 and α is the polarizability of the sphere of radius r.

$$\alpha = 4\pi r^3 \left( \frac{\varepsilon_m - \varepsilon_1}{\varepsilon_m + 2\varepsilon_1} \right) \qquad (2.1.3)$$

The efficiencies of extinction $\eta_{ext}$, absorption $\eta_{abs}$, and scattering $\eta_{sca}$ are obtained by dividing the cross sections due to light interaction by the geometric cross section of These efficiencies represent the ability of the particle to scatter light relative to its physical cross-sectional area.

Absorption cross section of the NP is strongly related to extinction coefficient as

$$\sigma_a = \frac{\varepsilon_\lambda \cdot m_a}{N_A} \qquad (2.1.4)$$

$N_A$ being Avogadro´s number. And $m_a$ the atomic mass

For a certain wavelength, we can obtain a value for the absorbance, and then find the extinction coefficient as follows

$$\varepsilon_\lambda = \frac{A_\lambda}{lc} \qquad (2.1.5)$$

For a laser with $\lambda = 632.8nm$ ,and a concentration of $c = 300 \frac{\mathrm{g}}{\mathrm{m}^3}$

$$\varepsilon_\lambda = \frac{A_\lambda}{lc} = \frac{2.609}{1 \cdot 300} \frac{m^3}{cm \cdot g} = 0.87 \frac{m^2}{g} \qquad (2.1.6)$$

The extinction coefficient, does not depend of the concentration of solution, for many concentrations of a same solution a same value for this coefficient is expected.

So, for $\lambda = 632.8nm$ we have a specific value for this coefficient, and so we can make some expected values for the absorbance of a substance at different concentrations.

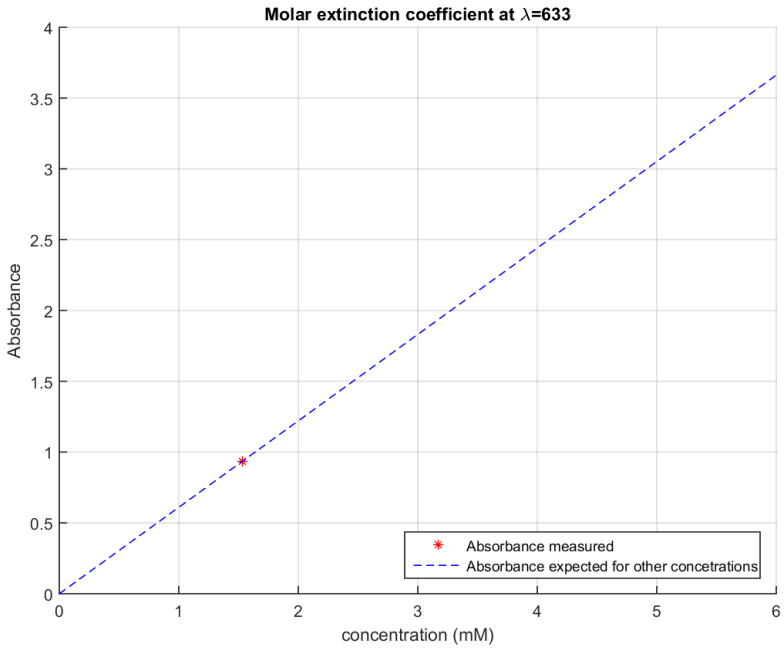


Fig 2.1 Molar extinction coefficient for different concentrations of the solution of gold hydrosol.

At the laser wavelength we have an absorption cross section

$$\sigma_a = \frac{\varepsilon_\lambda \cdot m_a}{N_A} = \frac{0.87 \cdot 197 \times 10^3}{6.022 \times 10^{23}} \frac{m^2 \cdot Mol \cdot g}{g \cdot Mol} = 28.46 \times 10^{-20} m^2 = 2846 nm^2 \qquad (2.1.7)$$

### 2.1.2 Heat Generation in Plasmonic Nanoparticles

The temperature increase in tissue is due a contribution of multiple nanoparticles, each one providing a certain amount of heat due its absorption cross section. The absorption cross section is an effective area. The absorption cross section can be larger than the geometric cross section.

According to Qin et al. (2012), the individual heat absorption

$$Q_{nano} = \sigma_a I \qquad (2.1.8)$$

for N number of nanoparticles in a certain concentration, the heat generation is commonly referred as specific absorption rate (SAR)

$$SAR = NQ_{nano} = N\sigma_a I = \mu_a I \qquad (2.1.9)$$

This equation contains important fundamental terms necessary for heat generation with GNPs and laser·

The NP absorb energy from the light source in order to convert it into heat, Takami et al.,(1999) reports that, for GNPs, the energy absorbed by the laser is calculated by

$$Q = \frac{E}{RCV} \qquad (2.1.10)$$

Where E is the laser energy absorbed by a hydrosol ($J^{s-1}$), R is the frequency of pulsed laser, C is the mass concentration of gold and irradiated volume V.

## 2.2 Multiscale Modeling of Temperature Distribution in a Media with Embedded Heating Nanoparticles

Three levels of modeling are used for the modeling of temperature distribution in hydrosol of NP, macroscopic, microscopic and nanoscale modeling. Macroscopic modeling refers as the system modeling as a whole. Describing temperature distribution for all surface or volume existing. The main assumption that is made in the case of microscopic modeling is the continuous distribution of heating sources, which can be described by a function Q(**r**,t).

The heat transfer in a system, consisting of heating NPs and a surrounding matrix is described by the usual heat transfer equation ,Avetisyan et al., (2010):

$$\rho(\vec{r})c(\vec{r})\frac{\partial T(\vec{r},t)}{\partial t} = \nabla k(\vec{r})\nabla T(\vec{r},t) + Q(\vec{r},t) \qquad (2.2.1)$$

where T(**r**,t) is temperature as a function of coordinate **r** and time t, ρ(**r**), c(**r**) and k(**r**) are the mass density, specific heat, and thermal conductivity, respectively.

The local heat intensity Q(**r**,t) comes from light dissipation in NPs.

Nano scale modeling describes the temperature distribution for a single NP and its surrounding media.

Most, if not all reports found in literature agree that the temperature distribution in a media with embedded heating nanoparticles is described by the heat transfer equation, but the parameters of such equation depend on the problem in question.

In the case of biological media, the heat transfer equation for the physical problem is changed to the known as Penne's bioheat equation

### 2.2.1 Macroscopic modeling

The superficial heat transfer from the nanoparticles to the media it is obtained by many authors in the literature as the model or a variation of the one reported in Richardson et al., (2009) as the solution for the energy balance equation from thermodynamics.

The work reported by Richardson et al starts with the energy balance equation

$$\sum_i m_i C_{p,i} \frac{dT}{dt} = Q_I - Q_{ext} \qquad (2.2.2)$$

Where the terms $Q_1$ and $Q_{ext}$ are the energy supplied by the laser to the solution, and energy dissipated by transfer to the exterior, respectively.

In this equation $m_i$ and $C_{p,i}$ are the mass and heat capacity components of the system, T is the temperature, and t is time.

The rate of energy supplied into the system is

$$Q_I = I\left(1-10^{-A_\lambda}\right)\eta \qquad (2.2.3)$$

where I is the incident laser power, $A_\lambda$ is the absorbance of the nanoparticle solution, and $\eta$ is the efficiency of converting light absorption to thermal energy.

The rate of energy loss out of the system is given by

$$Q_{ext} = hS\left(T - T_0\right) \qquad (2.2.4)$$

The parameter $\eta$ is obtained from the following equations:

$$\eta = \frac{Bm_w C_{p,w}\left(T_{ss} - T_0\right)}{I\left(1-10^{-A_\lambda}\right)} \qquad (2.2.5)$$

The efficiency of converting absorbed light to heat ($\eta$) is extracted from the experimental curves by solving this equation.

A simple macroscopic model was developed to describe the time dependence of surface temperature observed in the experiments. The model is similar to the ones previously published **[30,31]** and employs a heat generation in GNPs irradiated with light and its dissipation in water.

The following assumptions are made:

1. The incident photons are absorbed only by GNPs.
2. The rate of energy flowing out from the surface hydrosol layer is only convective.

3. The energy absorbed by GNPs dissipates in pico- to nanoseconds to a surrounding water and is distributed uniformly in the hydrosol.

The energy balance equation

$$\left(m_w c_w + m_{GNP} C_{GNP}\right)\frac{dT}{dt} = Q_I - Q_{ext} \qquad (2.2.6)$$

Here m and c are the mass and heat capacity of water and a GNP.

The energy balance equation can be re arranged to

$$\frac{dT}{dt} = A - B(T - T_{amb})$$
$$A = \frac{I_0\left(1-10^{-A_\lambda}\right)}{\left(m_w c_w + m_{GNP} c_{GNP}\right)} \qquad (2.2.7)$$
$$B = \frac{hS}{\left(m_w c_w + m_{GNP} c_{GNP}\right)}$$

Solving the energy balance equation for the cooling process (when the laser is turned off) yields to solve the equation

$$\frac{dT}{dt} = -B(T - T_{amb}) \qquad (2.2.8)$$

With the initial condition at $T_0=T_{max}$ the differential equation for temperature has the solution

$$T = T_{amb} + (T_{\max} - T_{amb}) \cdot e^{-Bt} \qquad (2.2.9)$$

The heating part is obtained from solve the equation, where

$$\frac{dT}{dt} = A - B(T - T_{amb}) \qquad (2.2.10)$$

The previous equation has a solution of the form

$$T = T_{amb} + \frac{A}{B}(1 - \cdot e^{-Bt}) \qquad (2.2.11)$$

Even though this model is not suitable for our system. It can be used with very good certain as a phenomenological description for our real system. For fixed points in our model. For example, it will be show that at the center of the surface (the point r=0, z=0), the previous model fits well with the experimental data acquired.

### 2.2.2 Microscopic modeling

The heat transfer equation governs the microscopic model of the system

$$c\ \rho\ \frac{\partial T}{\partial t} = \nabla \cdot (\kappa \nabla T) + Q(r,t) \qquad (2.2.12)$$

The parameters c, ρ and k are the specific heat, the density and the thermal conductivity of the material respectively.

The term Q is the volumetric heat source profile that is proportional to the light intensity. For the systems of interest is common to solve the equation with initial values problem.

It is of interest the study of the temperature profile in semi-infinity body both 1D and 2D. Being the 2D case the one that approaches the most to our system of study. In the next pages are described the theoretical reviews for 1D and 2D cases.

**1D case:**

An analytical solution for the temperature distribution in a semi-infinite body is calculated by Blackwell (1990). The system consists of a heat source that decays exponentially with position, and convective boundary conditions.

Equation (2.2.12) becomes, for the one dimensional case

$$c\ \rho\ \frac{\partial T}{\partial t} = \kappa \frac{\partial^2 T}{\partial x^2} + Q(x) \qquad (2.2.13)$$

The assumed boundary conditions are

$$-k \left. \frac{\partial T(0,t)}{\partial x} \right| = h\left[T_\infty - T(0,t)\right] \qquad (2.2.14)$$

and

$$\left. \frac{\partial T(\infty,T)}{\partial x} \right| = 0 \qquad (2.2.215)$$

By using Laplace transform methods it can be found a solution of the form

$$T - T_0 = (T_\infty - T_0)\left[ erfc\left(\frac{x}{2\sqrt{\alpha t}}\right) - \exp\left(\frac{h^2}{k^2}\alpha t + \frac{hx}{k}\right) erfc\left(\frac{x}{2\sqrt{\alpha t}} + \frac{h}{k}\sqrt{\alpha t}\right)\right]$$

$$+ \frac{I_0(1-R)}{\mu k}\left\{\left(1 + \frac{\mu k}{h}\right) erfc\left(\frac{x}{2\sqrt{\alpha t}}\right) + \frac{1}{\frac{h}{\mu k}\left(\frac{h}{\mu k} - 1\right)} \exp\left(\frac{h^2}{k^2}\alpha t + \frac{hx}{k}\right) erfc\left(\frac{x}{2\sqrt{\alpha t}} + \frac{h}{k}\sqrt{\alpha t}\right)\right.$$

$$- \frac{1}{2}\left(\frac{\frac{h}{\mu k} + 1}{\frac{h}{\mu k} - 1}\right) \exp\left(\mu^2 \alpha t + \mu x\right) erfc\left(\frac{x}{2\sqrt{\alpha t}} + \mu\sqrt{\alpha t}\right) - \frac{1}{2}\exp\left(\mu^2 \alpha t - \mu x\right) erfc\left(\frac{x}{2\sqrt{\alpha t}} - \mu\sqrt{\alpha t}\right)$$

$$\left. + \exp(-\mu x)\left[\exp\left(\mu^2 \alpha t\right) - 1\right]\right\}$$

(2.2.16)

for laser heating applications in which $I_0$ (1-$R$) is large in comparison to $h(T-T_0)$. For this case, a convenient group of dimensionless variables leads to the solution

$$\frac{T(\chi,\tau) - T_0}{\frac{I_0(1-R)}{k\mu}} = \frac{1}{\mu Bi}\left[ erfc\left(\frac{\chi}{2\sqrt{\tau}}\right) - \exp\left(Bi^2 + Bi\chi\right) erfc\left(\left(\frac{\chi}{2\sqrt{\tau}}\right) + Bi\sqrt{\tau}\right)\right]$$

$$+ \left(1 + \frac{1}{Bi}\right) erfc\left(\frac{\chi}{2\sqrt{\tau}}\right) + \frac{1}{Bi(Bi-1)} \exp\left(Bi^2 + Bi\chi\right) erfc\left(\frac{\chi}{2\sqrt{\tau}} + Bi\sqrt{\tau}\right)$$

$$- \frac{1}{2}\left(\frac{Bi+1}{Bi-1}\right) \exp\left(\tau + \chi\right) erfc\left(\frac{\chi}{2\sqrt{\tau}} + Bi\sqrt{\tau}\right) - \frac{1}{2}\exp\left(\tau - \chi\right) erfc\left(\frac{\chi}{2\sqrt{\tau}} - Bi\sqrt{\tau}\right) + \exp(-\chi)\left[\exp(\tau) - 1\right]$$

(2.2.17)

where

$$\tau = \mu^2 \alpha t$$

$$\chi = \mu x$$

$$Bi = \frac{h}{\mu k} \qquad (2.2.18)$$

$$\omega = \frac{I_0(1-R)}{h(T_\infty - T_0)}$$

are the dimensionless variables.

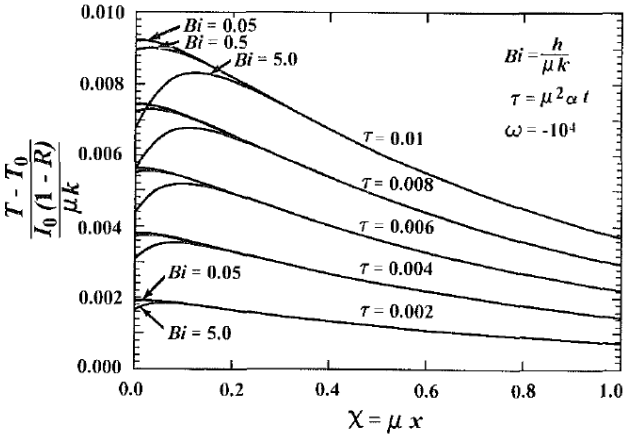


Fig. 2.2 Dimensionless temperature profile as a function of dimensionless space variable $\chi$ for various Bi and dimensionless times $\tau$ . Figure from Blackell (1990).

**2D case**

An analysis for the temperature distribution within the semi-infinity sample is presented in Sato et al., (2008) by solving the solution of the heat conduction differential equation (2.2.13).

with the initial condition T(r,z,0) = 0 and boundary conditions as T(∞,z ,t) = 0 and

$$\left.\frac{\partial T(r,z,t)}{\partial z}\right|_{z=0} = 0 \qquad (2.2.19)$$

The source profile for a Gaussian laser beam illumination is

$$Q(r,z) = Q_0 \exp\left(\frac{-2r^2}{\omega_{0e}^2}\right) Q(z) \qquad (2.2.20)$$

with

$$Q_0 = \frac{2P_e A_e \phi}{c_w \rho_w \pi \omega_{0e}^2} \qquad (2.2.21)$$

Where $A_e$, $P_e$ and $\omega_{0e}$ are the optical absorption coefficient at the excitation beam wavelength, the excitation beam power, and the probe beam radius respectively.

In this work, it is considered three cases for the z-dependence of the source term:

$$Q(z)=\begin{cases}1, & LAM\\ \exp(-A_e z), & BLM\\ \dfrac{2}{A_e}\delta(z), & HAM\end{cases} \qquad (2.2.22)$$

Here HAM denotes a high absorbing model while LAM stands for low absorbing model. The Beer's law model (BLM) assumed here can be used to describe the induced effects in the sample in the whole absorption coefficient range. On the other hand, the low and high absorption limits can be used to describe the same effects in the extremes of the absorption coefficients, bringing mathematical simplicity to the theoretical models presented in their work.

By using the integral transform methods, in the Laplace, Fourier cosine, and Hankel space, the solution of the heat conduction differential equation for each case can be written as

$$T_{LAM}(r,z,t)=T_0\int_0^t \frac{2A_e\exp\left(-\dfrac{2r^2/\omega_{0e}^2}{1+2\tau/t_c}\right)}{\omega_{0e}^2(1+2\tau/t_c)}d\tau \qquad (2.2.23)$$

$$T_{BLM}(r,z,t)=T_0\int_0^t \frac{A_e\exp\left[\left(A_e\tau\omega_{0e}^2/t_c-4z\right)/4\right]}{\omega_{0e}^2(1+2\tau/t_c)}\times\exp\left(-\frac{2r^2/\omega_{0e}^2}{1+2\tau/t_c}\right) \qquad (2.2.24)$$
$$\times\left[erfc\left(\frac{A_e\tau\omega_{0e}^2-2zt_c}{2\sqrt{\omega_{0e}^2\tau t_c}}\right)\times\exp(A_e z)erfc\left(\frac{A_e\tau\omega_{0e}^2+2zt_c}{2\sqrt{\omega_{0e}^2\tau t_c}}\right)\right]d\tau$$

$$T_{HAM}(r,z,t)=T_0\int_0^t \frac{4\exp\left(\dfrac{z^2t_c}{\omega_{0e}^2\tau}\right)\exp\left(-\dfrac{2r^2/\omega_{0e}^2}{\omega_{0e}^2\tau}\right)}{\sqrt{\pi}\sqrt{\dfrac{\omega_{0e}^2\tau}{t_c}\omega_{0e}^2\left(1+2\tau/t_c\right)}}d\tau \qquad (2.2.25)$$

| | $TiO_2$ | | |
|---|---|---|---|
| | 0.5 wt % | 2.5 wt % | 3.5 wt % |
| $P_e$ (mW) | 20 | 20 | 20 |
| $A_e$ ($m^{-1}$) | 77 | 544 | 1061 |
| $D$ ($10^{-3}$ $cm^2/s$) | 6 | 6 | 6 |
| $k$ (W/mK) | 1.5 | 1.5 | 1.5 |
| $\omega_{0e}$ ($\mu$m) | 44 | 44 | 44 |
| $t_c$ (ms) | 0.81 | 0.81 | 0.81 |
| $\phi$ | 0.87 | 0.70 | 0.72 |
| $\alpha_T$ | 7.7 | 7.7 | 7.7 |
| $\nu$ | 0.29 | 0.29 | 0.29 |

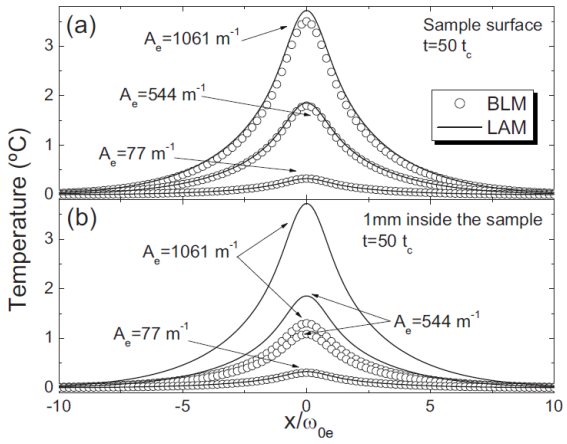


Fig. 2.3 Table of parameter used in Sato et al.,(2008) for the simulation (left) Temperature profile for $TiO_2$ doped LSCAS glasses at the sample surface (right a) and inside (right b ). LAM is simulated in lines while BLM with circles.

From the results presented by sato et al., (2008), a radial temperature distribution (RTD) can be noticed both, at the surface and inside the sample with a maximum of temperature at the center of the beam.

### 2.2.3 Nanoscale model

Now it is interesting to see the temperature distribution at a system in the surroundings of a single nanoparticle. This is how the nanoparticle transfers heat to water.

The time scale for thermal processes are in the order or 10 ns to 10000 ns, Donner et al., (2014). For this typical times a steady state for the heat transfer equation can be assumed. In such regime the equation becomes

$$\kappa \nabla^2 T(r) = Q(r) \qquad (2.2.26)$$

The Poisson equation. For plasmonic structures like nanoparticles the heat generation Q is non-uniform but its internal temperature is. It remains in a quasi-uniform state. So the equation for the surroundings of a nanoparticle becomes

$$\kappa \nabla^2 T(r) = 0 \qquad (2.2.27)$$

The Laplace equation. Which leads to a solution for temperature that decreases while r increases.

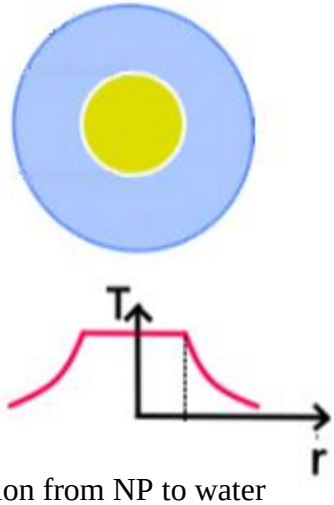


Fig. 2.4 Temperature distribution from NP to water

Pustavalov et al. (2005) makes a study about the heating of spherical nanoparticle in medium on exposure to laser radiation pulse and following cooling is considered on the base of analytical solutions. The time dependencies of particle temperature are obtained. And makes a comparison of some predicted results of the heating of gold spherical nanoparticle in liquid media with experimental data and found an agreement of theoretical results with experimental data, validating the model and theory developed.

Kryachko et. al.,(2010) reported model to assess the thermal effect of the absorption of the energy pulse of coherent microwave radiation by the conducting nanocluster surrounded by a liquid medium. The free electron maser is considered as the source of radiation. Examples of calculations based on this model are presented. The possible effect that microwave therapy with the use of nanoclusters might have on treating cancer is assessed.

From the statements of Khlebtsov et al (2006) and in accordance to Pustovalov et al., (2005); the temperature increment of nanoparticles, if all optical energy is used to heating the particles, can be evaluated as

$$\Delta T \approx \frac{FC_{abs}}{km} = \frac{FQ_{abs}}{c\rho_g R_g},$$

where F is the average laser fluence, $C_{abs}$ is the absorption cross section, m is the gold mass of the particle, c is the specific heat of gold, $\rho_g$ is the gold density, Rg is the radius (or equivalent radius for nanorods), and

$$Q_{abs} = \frac{C_{abs}}{\pi R_g^2},$$

is the normalized absorption cross section of spheres or nanorods.

## 2.3 Experimental Measurements of the Light-to-Heat Conversion

There are many methods for measuring temperature. In the field of light to heat conversion for nanoparticles the most common methods are the thermocouple and the IR thermography.

### 2.3.1 Thermocouple Measurements

The principal advantage of the thermocouple method is that it provides a direct measurement of the system due its invasive characteristic. But at the same time that characteristic makes it somehow uncomfortable to use for many systems.

It can be found in literature that the use of thermocouple for the temperature measurement is a common practice. An example of this kind of measurements is the one reported by Richardson et al., (2009). Their experiment consist in a droplet of water with a thermocouple inside and a laser beam going through the droplet ( see figure below )

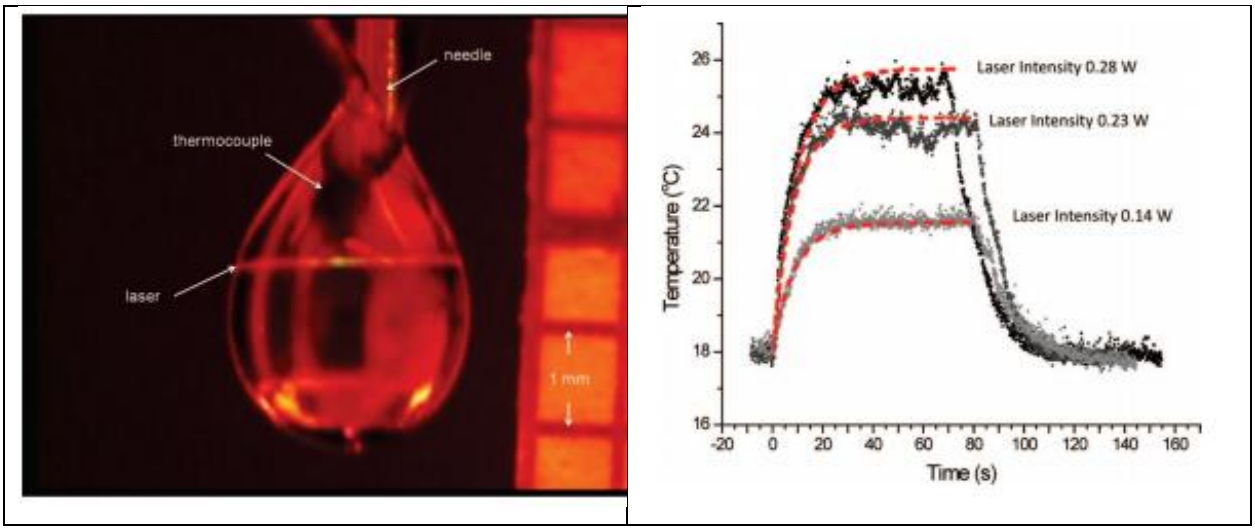


Fig. 2.5 Experimental set up used by Richardson et al.,(2009) for the measurement of temperature distribution using thermocouple (left). Results reported by Richardson et al. The time dependent temperature distribution behavior for the heating stage and the cooling stage are similar for those reported with another measurement mechanisms. (right).

The results for their experiment are consistent with the results for other experiments using another mechanisms to measure temperature distribution. The regimen worked in this article is the macroscopic modeling.

Roper et al., (2007) conducted experiments to obtain the effects of laser power, the dimension and shape of AuNPs on the photothermal conversion efficiency. The behavior of the results exhibit are in accordance with those showed from other investigations.

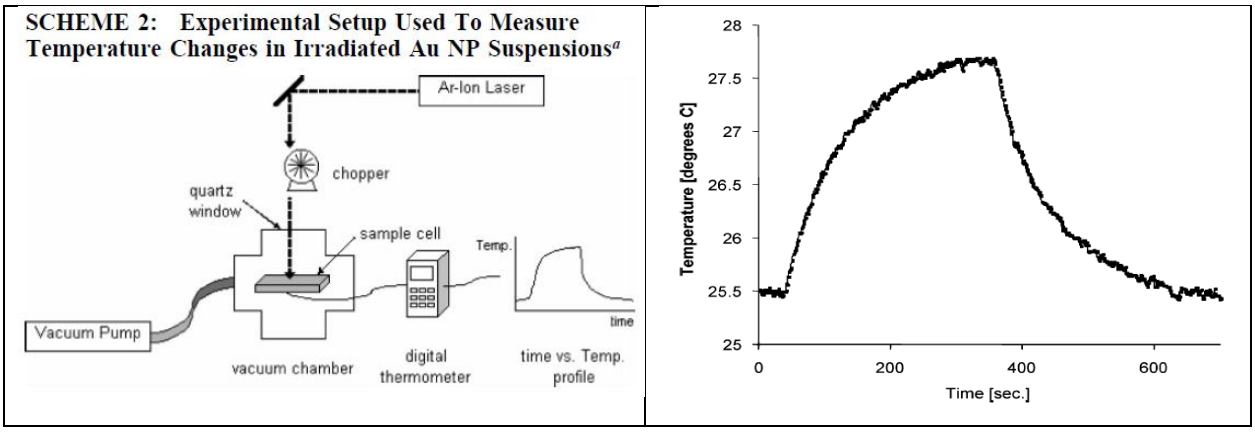


Fig. 2.6 Scheme 2 (left) shows the experimental layout. A cw Ar+ ion laser (514 and 488 nm, BeamLok 2060&2080, Spectra-physics, Mountain View, CA) was used to irradiate the sample

through a quartz window in the vacuum chamber. Plot (Right) exhibit results from temperature changes measured with thermocouple.Figure from Roper et al.,(2007).

As stated before, the streng of this method is the ability to measure temperature dristribution inside the system under study. Example of this are the results presented by An et al., (2012).

Their results are from an experimental system (shown in Fig. 2.5 top left) constructed to investigate the temperature distribution of GNRs irradiated by a continuous-wave laser. Solutions are contained in a plastic cylindrical tube covered with insulating material except for the top surface. Five thermocouples are arranged inside the tube along the vertical axis to measure the temperature distribution on z direction, and the other three thermocouples are arranged at different locations on the same horizontal plane to measure the temperature distribution in the radius direction (Fig. 2.5 top right).

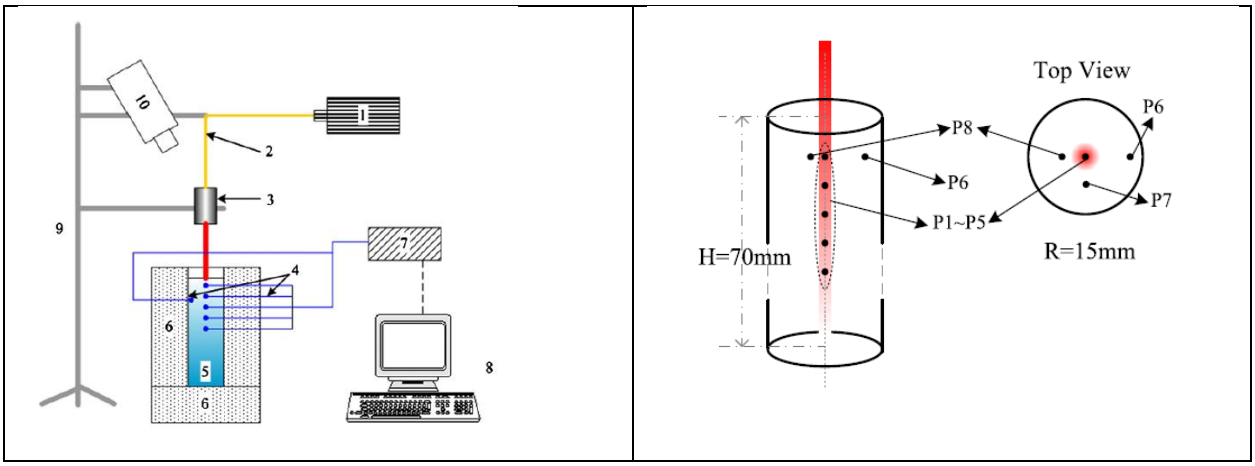

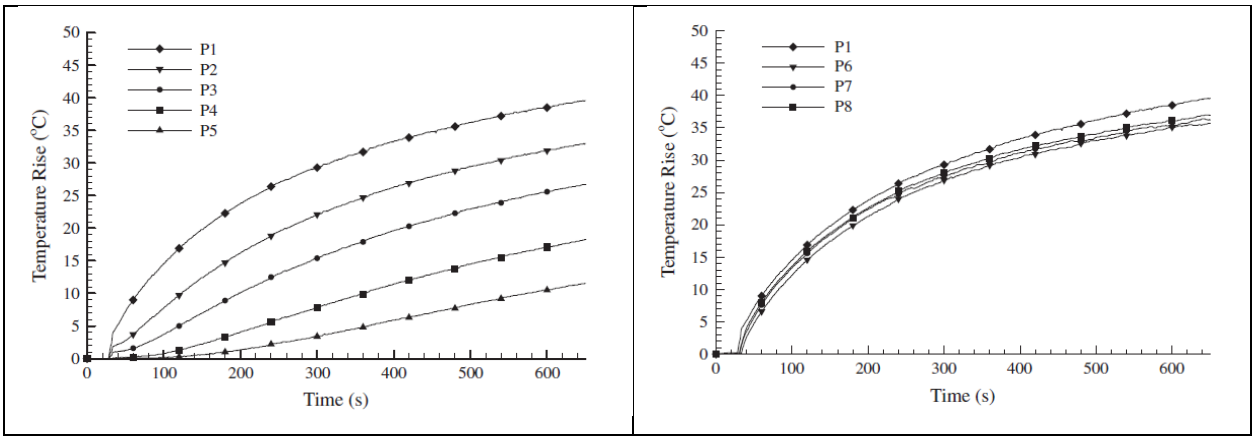


Fig. 2.7 Top left shows experimental array. Top right shows the points of measurement of thermocouples. Bottom figures are the data results from experiment at the different points. Image taken from An et al., (2012)

### 2.3.2 IR thermography Measurements

IR thermography is a method, which detects IR energy emitted from objects, converts it to temperature values, and displays an image of temperature distribution for such objects. The equipment to do IR thermography is known as IR thermograph.

Some of the advantages of the use of IR thermography is that can make an image for the temperature distribution in real time. And unlike thermocouples, temperature can be measured from a distance without contacting the object.

Li et al., 2017 developed a procedure to measure light to heat conversion efficiency of a 2-d material MXene with a droplet light heating system.

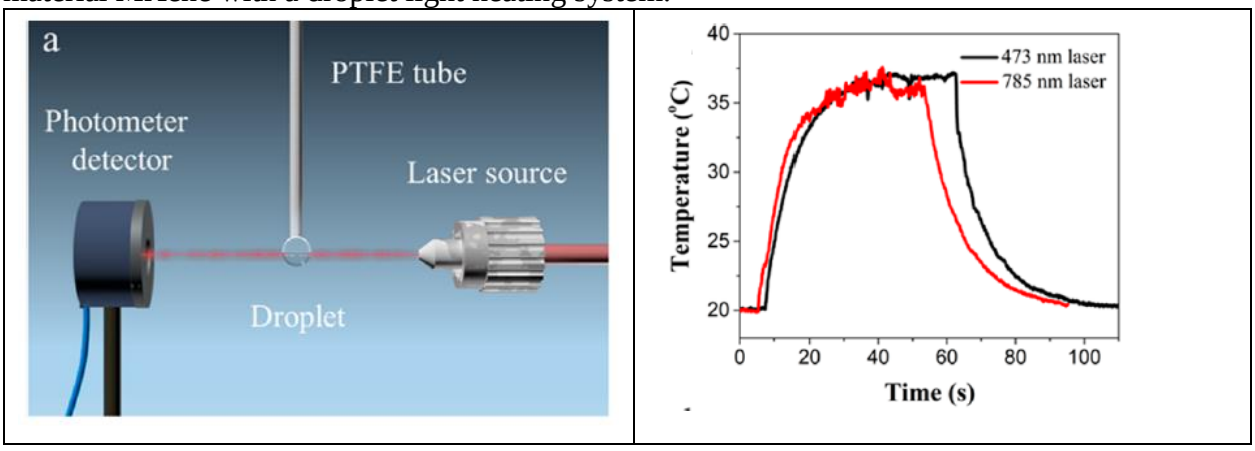

Fig. 2.8 Image from Lie et al.,(2017). On the left is the experimental set up used in the investigation. Results of temperature increase when MXene irradiated with 2 different wavelengths (right).

Akchrin et al., (2007) also use IR thermography to visualize the influence of laser pulse on GNPs water or salt solution temperature change.

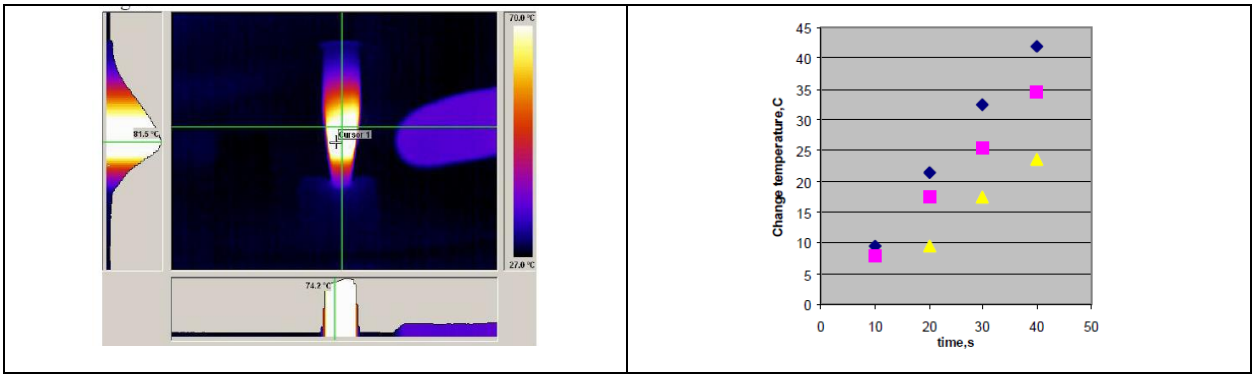


Fig 2.9 Thermograph of the solution irradiate with light(left). Right figure shows results of pulse laser heating of resonant nanoshells with typical plasmon resonant on wave length 800 nm (average laser power 2W) and pulse duration 10 ms (blue); 1 ms (pink) and 200 μs yellow). Results from Akchrin et al.,(2007).

As stated before IR thermography has applications in the field of medicine. There are many works on hyperthermia for cancer treatment. Such works rely on the non-invasiveness of IR thermography.Investigation of thermal effects and alterations of tissue morphology induced by laser irradiation at subcutaneous and/or intramuscular injection of 0.1-ml silica/gold nanoshell suspensions was carried out using white laboratory rats ,Terentyuk et al., (2009). An IR thermograph was used for noninvasive monitoring of surface in solution of designed silica/gold nanoshells

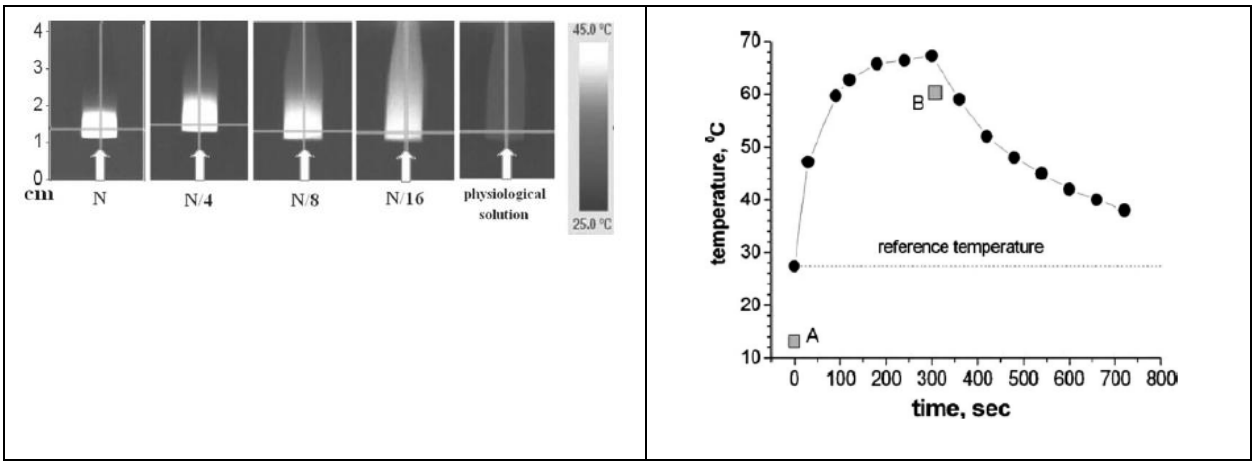


Fig. 2.10 Figures from Terentyuk et al., (2009) shows temporal dependence of temperature in the center of the laser spot of the continuous wave diode laser (810 nm) used for heating the solution of GNPs with a concentration of $N=5x10^9$ $cm^{-3}$ in the test tube (right). Thermal images for the heating of the Nano shell solutions at different concentrations(left).

experiments with the laser heating of GNP allow for determination of such important parameters as the level of IR laser power density and the corresponding temperature increment caused by nanoparticles in solutions irradiated by CW or pulsed laser light., Maksimova et al., (2007)

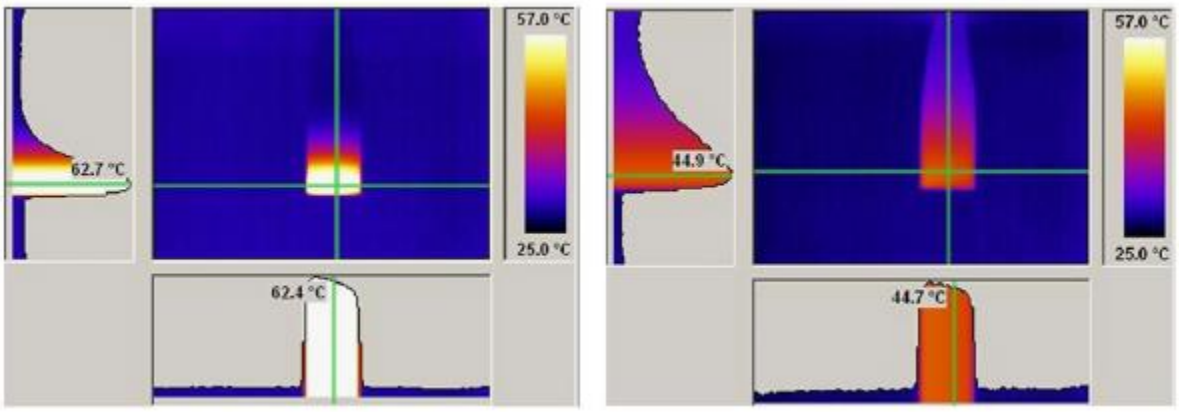


Fig 2.11 Thermogram of plasmon-resonant nanoshells in a standard Eppendorf tube after 2 min irradiation with a laser beam power of 2W: (left) Particle concentration is $5x10^9$ $ml^{-1}$ and (right) particle concentration was decreased to $0.61x10^9$ $ml^{-1}$. The incident light propagates from bottom to top.From Maksimova et al., (2007).

Tsao et al., (2015) investigated the light heating of Au films under broadband illumination from LED and halogen lamps. By using a thermographic camera to record the sample temperature in real time, so it could observe directly, variations in photothermal heating arising from the NP diameter, NP concentration, irradiation intensity, and type of light source.

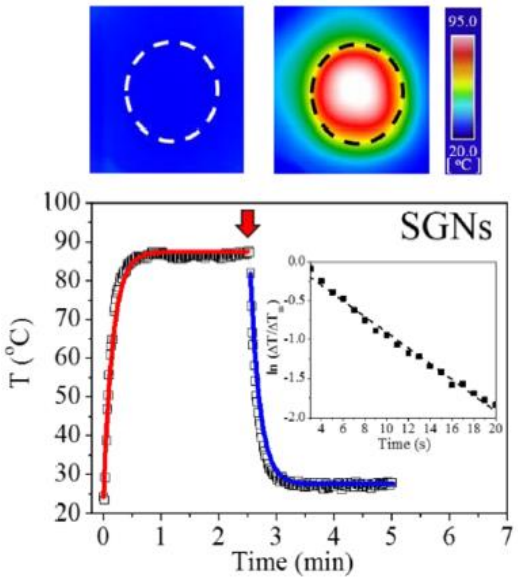


Fig. 2.13 Results from Tsao et al., (2015).Typical thermal images of SGN/ (top). Temperature variation over time (bottom).

### 2.3.3 MRI measurements

There are found in literature other techniques for measure temperatures from IR radiation. Magnetic resonance thermometry studied in Hirsch et al., (2003) can be used for treatment planning, localization, and monitoring of the temperature distribution during the treatments.

Histological examination revealed that MRI temperature estimation of tissue damage was in good agreement with experimental findings, demonstrating its potential utility in determining tissue damage during therapy.

### 2.3.4 Fluorescence measurements

Fluorescent thermometry is another method for measure temperature variations in a system. The studies of Chiu et al., (2015) have established experimental and analytical methods to illustrate the photothermal transduction efficiency of GNPs using a temperature-sensitive fluorescing molecule as an in-situ thermometer.

# CHAPTER 3

# IR THERMOGRAPHY STUDIES ON 632 NM LASER HEATING OF GOLD NANOPARTICLES IN WATER

In this chapter, we describe a novel IR thermography method of study on the photothermal effect in plasmonic nanoparticles immersed in dielectric media illuminated with light. As a model system was chosen a water colloid of GNPs (gold hydrosol) under continuous wave illumination with a 632 nm laser. The first subchapter describes the synthesis of hollow GNPs and optical properties of the gold hydrosol. The second subchapter is devoted to the description of the experimental measurement of the light-to-heat conversion by the IR thermography methods. Pre-processing of IR images and evaluation of the temperature distributions in the near-surface layer are presented in the third subchapters.

## 3.1 Hollow Gold Hydrosol

### 3.1.1 Synthesis of Hollow Gold Nanoparticles

Hollow nanoparticles were prepared via the well-established templated galvanic replacement reaction of silver for gold following the method reported by Prevo et al., (2008) with slight modifications (Carrillo et al., 2016). Silver nitrate ($AgNO_3$, ≥ 99%), sodium citrate dihydrate ($Na_3C_6H_4O_7 \cdot 2H_2O$, ≥ 99%), sodium borohydride ($NaBH_4$, ≥ 96%), hydroxylamine hydrochloride ($NH_2OH \cdot HCl$, ≥ 99%), gold (III) chloride trihydrate ($HAuCl_4 \cdot 3H_2O$, ≥ 99.9%) were purchased from Sigma-Aldrich Co. (St. Louis, MO) and used as received. All glassware was washed with soap, aqua regia, rinsed several times with tap water and deionized water. Ultrapure water with a resistivity of about 18 MΩ·cm was used.

The synthesis consisted of three stages. Firstly, 1 mL of sodium borohydride (100 mM) was added to 50 mL of an aqueous solution containing silver nitrate (0.6 mM) and sodium citrate (0.5 mM) under vigorous stirring at 60°C during 2 hours, to ensure complete hydrolysis of sodium borohydride. Next, the reaction mixture was cooled to room temperature and 1 mL of 200 mM hydroxylamine hydrochloride was added followed by stirring during 5 minutes. After that, 0.375 mL of silver nitrate (100 mM) were added and mixed during 2 hours. Finally, the silver nanoparticle solution was heated to 60°C and 0.5 mL of chloroauric acid (25 mM) were added

under vigorous stirring and left to react during 10 minutes. The silver solution changed its color immediately from yellow-orange to dark blue after the addition of gold. After the reaction time elapsed, the stirring was stopped and the reaction flask was left to cool to room temperature during night. To eliminate silver chloride produced during the reaction, the entire volume was centrifuged at 3500 rpm during 15 minutes and the pellet was discarded. Nanoparticles were washed two times with water by centrifugation at 5000 rpm during 60 minutes. The final pellet was resuspended in calculated amount of water forming a gold hydrosol of needed concentration.

### 3.1.2 Characterization of the Gold Hydrosol

Fig. 3.1.1 presents a representative transmission electron microscopy (TEM) image of synthesized hollow GNPs. From the image, it is clear that the gold particles are hollow shells. The radius, R and wall thickness h of the particles are about of 30 and 10 nm, respectively.

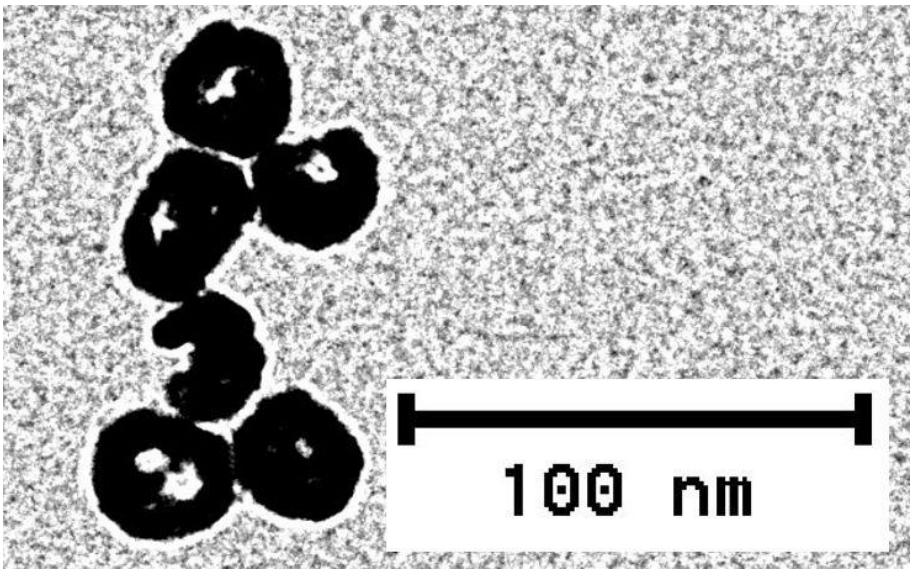


Fig 3.1.1 TEM images of GNPs. The center of each particle is relatively electron transparent, indicative of a hollow center, showing that the silver template nanoparticle was converted to molecular silver.

The optical absorption experiment was carried out with a Perkin Elmer Lambda 20 spectrometer in the wavelength range from 400 to 850 nm using disposable polystyrene cuvettes with an optical path, l of 1 cm and a scanning velocity of 120 nm/min. Fig. 3.1.2 shows the absorbance of the hollow GNP hydrosol, which was used in this work for the study on the photo

thermal effect. The total mass concentration of gold, $C_{Au}$ was determined by the hydrosol evaporation to be 0.3 mg/mL. Considering that the average diameter and wall thickness of the particles measured using TEM are about of 13 and 10 nm, the average mass of one hollow GNP, $M_{GNP}$ can be estimated (see subchapter 3.3.1) as $1.7\times10^{-19}$ kg. The GNP concentration, $n_{GNP} = C_{Au}/M_{GNP}$ is about $1.7\times10^{18}$ particle/$m^{-3}$.

The optical absorption and scattering of nanoparticles are characterized by absorption cross section and scattering cross section, $\sigma_a$ and $\sigma_s$, respectively. The Beer–Lambert law relates the absorbance, A to the extinction cross section, $\sigma_{ex} = \sigma_a + \sigma_s$ as

$$A = n_{GNP}\sigma_{ex}l = n_{GNP}\sigma_a l / f_a . \qquad (3.1.1)$$

where $f_a = \sigma_a/\sigma_{ex}$ is the relative absorption efficiency of the GNP (a measure of how much of the nontransmitted light is absorbed rather than scattered).

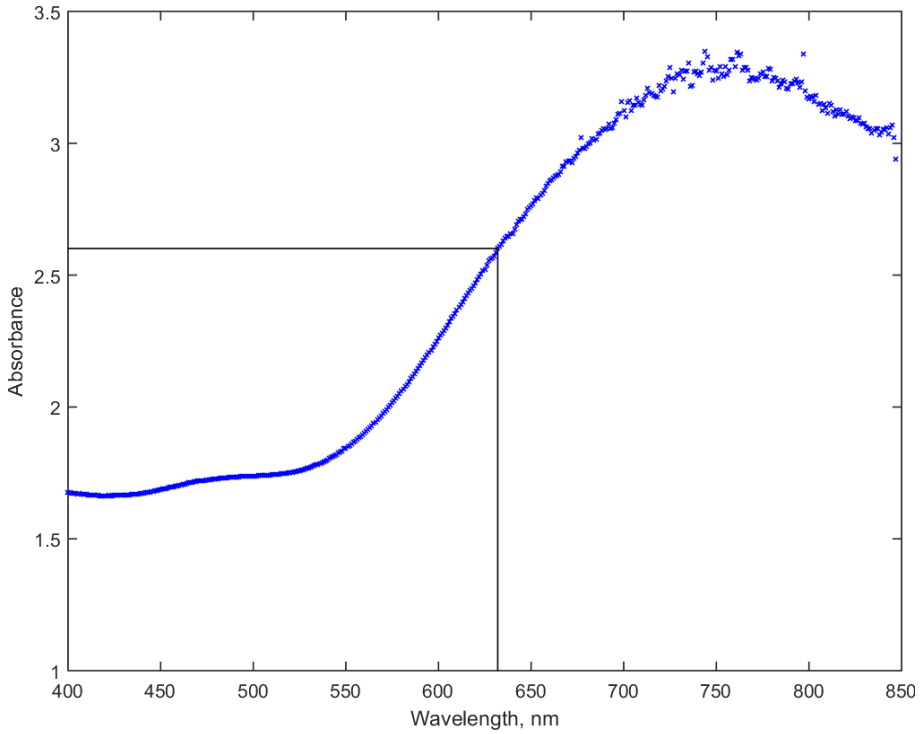


Fig 3.1.2. Absorbance spectrum of the hollow GNP hydrosol with the concentration of 1.1×1012 particle/cm-3. The black lines indicate the wavelength of the laser stimulation light, 632 nm and the corresponding absorbance that is 2.6.

Direct Mie calculations provided by Prevo et al., (2008) have shown that $f_a$ are closed to unity and for a 7-nm wall thickness hollow GNPs with diameters of 30 and 50 nm are equal to 0.95 and 0.9, respectively. Assuming $f_a = 0.9$ we can find from Eq. 3.1.1 that absorption cross section of the hollow GNPs for the laser laser stimulation light of 632 nm is about $2.0\times10^{-12}$ cm$^2$. Taking into account that the cross-section area of the GNP, $S_{GNP} = \pi R^2$ is equal to $7.0\times10^{-12}$ cm$^2$, the absorption efficiency, $\eta_a = \sigma_a/S_{GNP}$ was found to be 0.3.

## 3.2 IR measurements of Light-to-heat Conversion

### 3.2.1 IR Measurements

The light-to-heat conversion measurements were carried out using a simple experimental setup schematically shown in the left panel of Fig. 3.2.1.

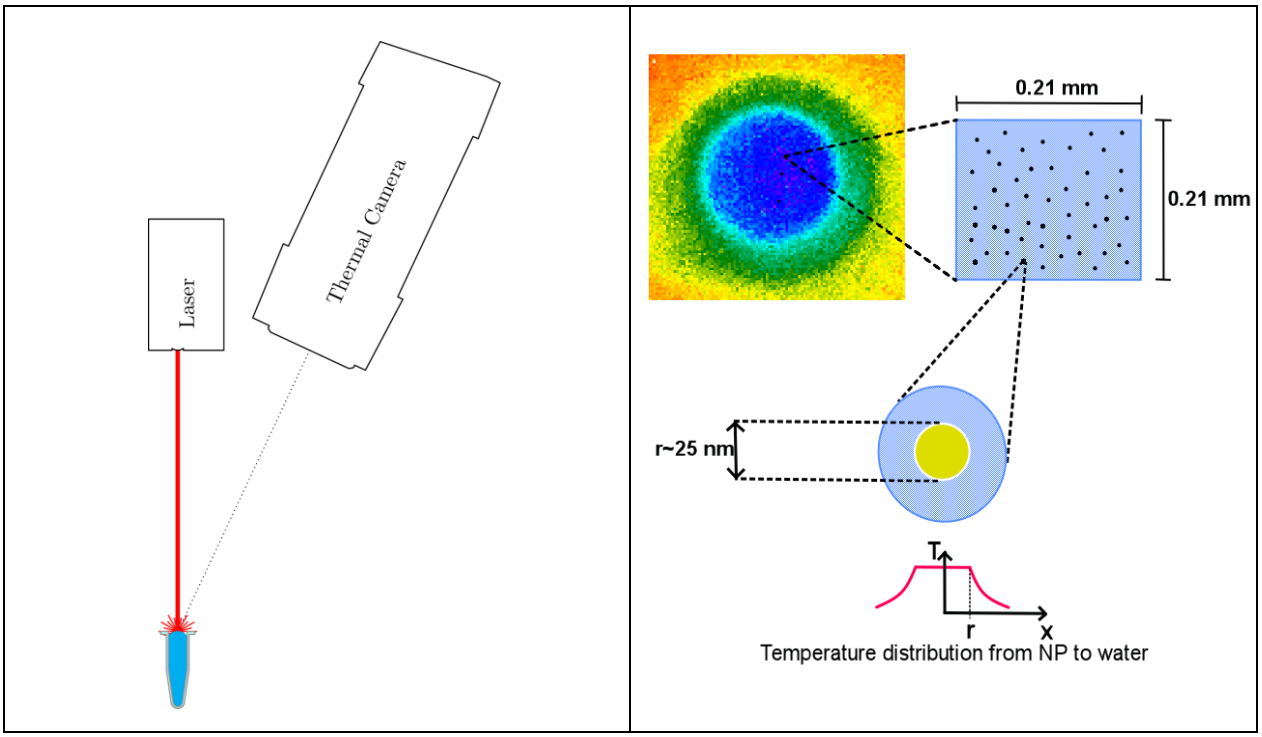


Fig 3.2.1. (a) Experimental setup for the light-to-heat conversion measurements. (b) Typical dimensions of: IR image of Eppendorf tube with the hydrosol; one pixel of the image; radial temperature distribution around GNP.

The laser used for the hydrosol illumination was a continuous-wave Melles-Griot He-Ne laser with a wavelength of 632.8 nm and output power of 30 mW. The laser light was delivered through an optical fiber falling normally on the hydrosol surface. The distance between the end of the fiber and the surface was about 30 mm. The surface temperature was monitored in a continuous way using a FLIR SC655 IR camera (spectral range 7.5-13 μm, resolution 640 × 480 pixels) focused on the hydrosol surface. The IR camera is connected to the computer with installed FLIR's ThermaCAMR RTools™ software, which can serve a wide variety of functions from real-time image acquisition to post-acquisition analysis. The camera was placed almost perpendicularly to the surface to avoid viewing angle error and the distance between the camera and the surface was maintained at about 30 cm. The horizontal and vertical spatial resolution of the recorded IR images were found to be 0.21 mm/pixel. The hydrosol surface emissivity was considered to be 0.98 (as for pure water).

The gold hydrosol was placed into 1.5 ml Eppendorf tube, which was vertically positioned in a closed thermoisolated box with two holes. Through the first small hole the fiber was introduced into the box. The second hole was used for the hydrosol surface IR imaging. After putting the Eppendorf tube with the hydrosol into the box and adjusting the optical fiber and IR camera, the box was kept untouched during about 10 min to reach a temperature equilibrium. Then the IR camera was switched on and the image sequence of 21 images was acquired at the time interval of 2 s. The first five images (10 s) were taken without laser illumination, then the laser was switch on and ten images (20 s) were recorded, the last five images (10 s) were again taken without laser illumination.

### 3.2.2 Pre-processing of IR images and visualization the heated area

Once the thermal camera recollect a set of IR images before during and after laser illumination, it was needed a program to analyze such information. Using MATLAB as the code language, a simple software was created to manipulate the information obtained in the experiment. Such program can work with any kind of experiment related to thermal cameras and superficial temperature effects.

ThermaCAMR RTools™ software can save images in a number of formats. The most appropriate for us is FLIR Public Format (FPF) files with extension *.fpf allowing users to

perform analysis on the raw image data using custom analysis software. The FPF ffile consists of a header followed by a matrix of single precision IEEE floating point values, each representing one temperature point on the image. The thermal images analysis of our experiment is treated with the MATLAB software. A code was created to analyze data from experiment in a simple and straightforward way. The MATLAB code includes a certain number of steps.

From the experiments it were obtained an approximated number of 21 .FPF files per experiment depending on the frequency of images taken per second. Due to .FPF format size ,it was almost obligatory to transform such files into a much more portable format such as .CSV. , So the first thing in the program code does precisely that.

Below the step-by-step description of the procedures used for the visualization of the heated area from a set of IR images is presented.

Load *.fpf files (FLIR format), transform them into temperature arrays and select processing area (which includes the Eppendorf tube surface only).

The Flir images are loaded one by one into the program to obtain each temperature array in order to select an area that only includes the Eppendorf tube. From each temperature array obtained before, it is needed the maximal and minimum temperature in order to obtain a scale of temperature to show the image and select the region of interest. Because of the mount of the experiment is fixed, the region of interest for all images is always the same. In the coordinates of the MATLAB code the area is fixed in the rectangle rect = [213,120,107,90]. With this information, all images reduce to the area within such rectangle.

With this it is eliminated a bunch of data that is useless for the study and the data left contains precisely the region of interest of the experiment Once the files are cropped a new scale is made by identifying the new minimal and maximal temperature.

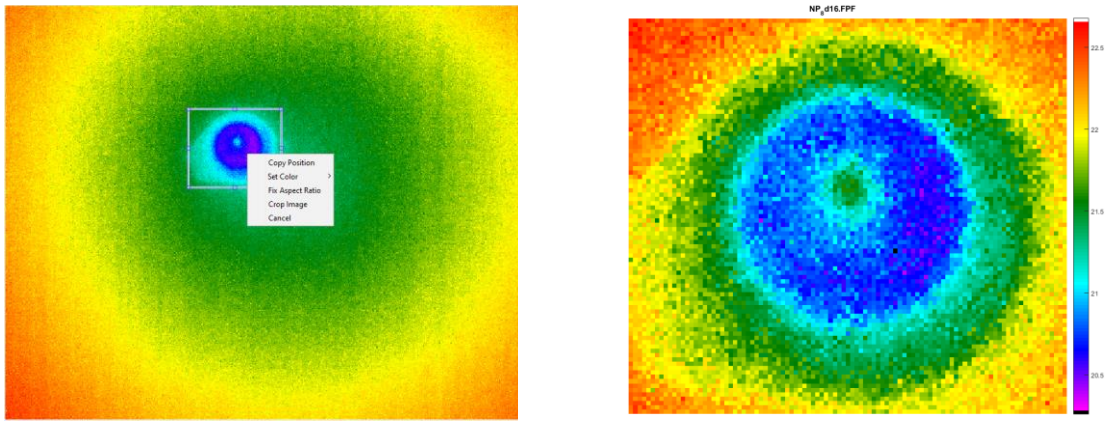


Fig. 3.2.2 Left: the maximally heated image (n = 16) with the selected rectangle, which includes the Eppendorf tube surface only. Right: The image cropped from the left image with the rectangle rect = [213,120,107,90].

**Image acquisition with FLIR SC655 IR camera**

Connect the IR camera to the PC and start the ThermaCAM™ Researcher Professional program

Determine the number of background ($n_b$), heating ($n_h$) and cooling ($n_c$) images and the time interval for recording one image ($t_1$, s)

Set the image recording conditions

Start the image recording

Wait $n_b t_1$ seconds and switch on the laser

Wait $(n_b + n_h)t_1$ seconds and switch off the laser

Save recorded images in the FLIR Public Format (*.fpf)

**Initial pre-processing of the infrared images**

One by one automatically load FPF images files and transform them into raw temperature arrays

Manually select a crop rectangle containing only the Eppendorf tube surface

Crop the raw temperature arrays and save the cropped arrays $\mathbf{T_{b,i}}$, $\mathbf{T_{h,j}}$, $\mathbf{T_{c,k}}$, where i = 1, 2, …, $n_b$, j = 1, 2, …, $n_h$, and k = 1, 2, …, $n_c$, respectively for future processing

Fig. 3.2.3 Flowchart for the image data acquisition and the pre processing of IR images.

## 3.3 Evaluation of Temperature Distributions

### 3.3.1 Visualization of the Heated Area

In order to processing the area of heating, it is need a way to find this area specifically within the picture. The right panel of Figure 3.3.1 shows the temperature variation during the experiment in the surface point indicated on the left panel. The point marked as 'Heated area' is located inside the laser beam while the point 'Background 1' and 'Background 2' are not subjected to the illumination. It is possible to see that the temperature variation inside the heated area between 10 and 30 s (the time when the laser was switched on) is obviously higher than in the non-heated area. This observation give a possibility to visualize the heated area. It is logically to suppose that the standard deviation (SD) of the temperature variation calculated during a laser illumination should be higher for the points located inside the heated area in comparison with the other ones.

For a selected set of temperatures at a given point i, j, $T(t_k,i,j)$, the SD is defined as

$$SD(i,j)=\sqrt{\frac{1}{N-1}\sum_{k=1}^{N}\left[T(t_k,i,j)-T_{meam}(i,j)\right]^2}\,, \qquad (3.3.1)$$

where $T_{mean}(i,j)$, is the mean of the selected set:

$$T_{meam}(i,j)=\frac{1}{N}\sum_{k=1}^{N}T(t_k,i,j) \qquad (3.3.2)$$

and $t_k$, $k = 1,\ldots,N$ are the time at which the images were taken, N is the number of the images.

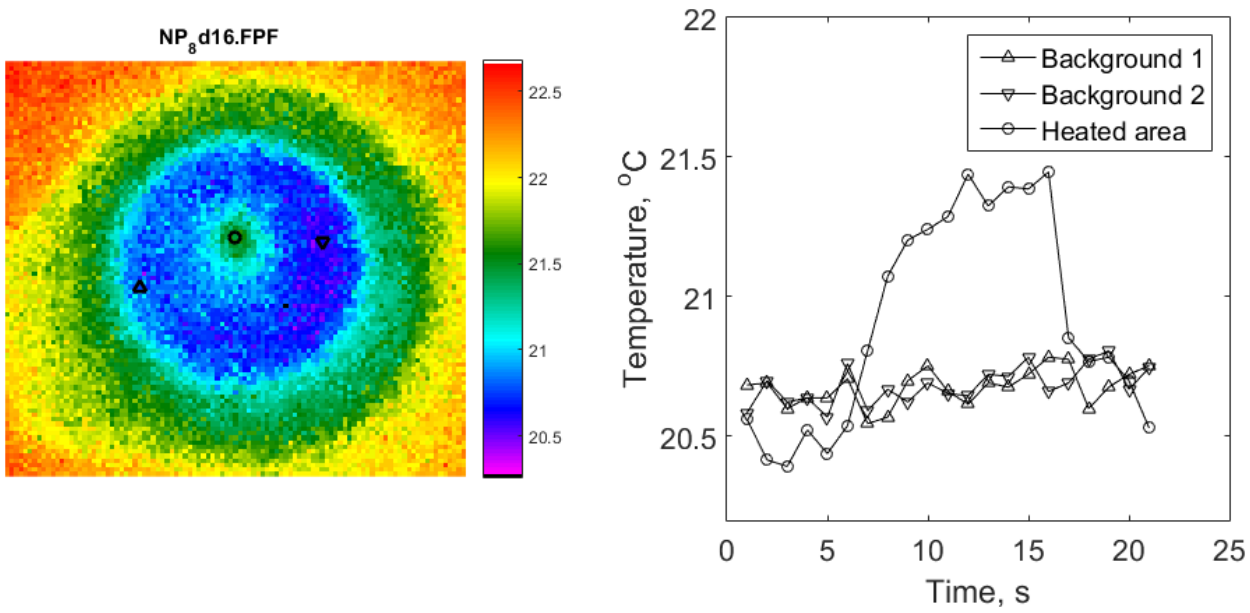


Fig. 3.3.1. Left: the temperature distribution over the hydrosol surface taken immediately before switch off the laser (maximal heating). Right: the temperature variation during the experiment in the surface point indicated on the left panel.

Figure 3.3.2 shows the images taken at the start and the end of the illumination as well as the distributions of $T_{mean}$ and SD evaluated with Eqs. (3.3.1) and (3.3.2) for $t_k$ between 11 and 30 s, which presents the mean temperature and its SD over the hydrosol surface during laser illumination. It is possible to see that both the image with maximal heating and the image with mean temperature exhibit heated area. The most pronounced effect of the illumination is observed for the SD image, on which the heated area is seen very clear as an area of yellow and red color.

### 3.3.2 Detection of the hot zone and its center

For the quantitative evaluation of the light-to-heat conversion in the hydrosol, it is needed to know the position of the laser beam. Because an IR image does not show the laser light reflected from the surface, the only way to localize the beam position on IR images is the quantitative analysis of the temperature distribution over the hydrosol surface.

As was mentioned above, the increased values of SD indicate very clear the position of the laser beam. Moreover, the laser-illuminated area is the only area that exhibit significant increasing

of the temperature variation. It is logically to suppose that the laser beam center located near the pixels with the maximal SD.

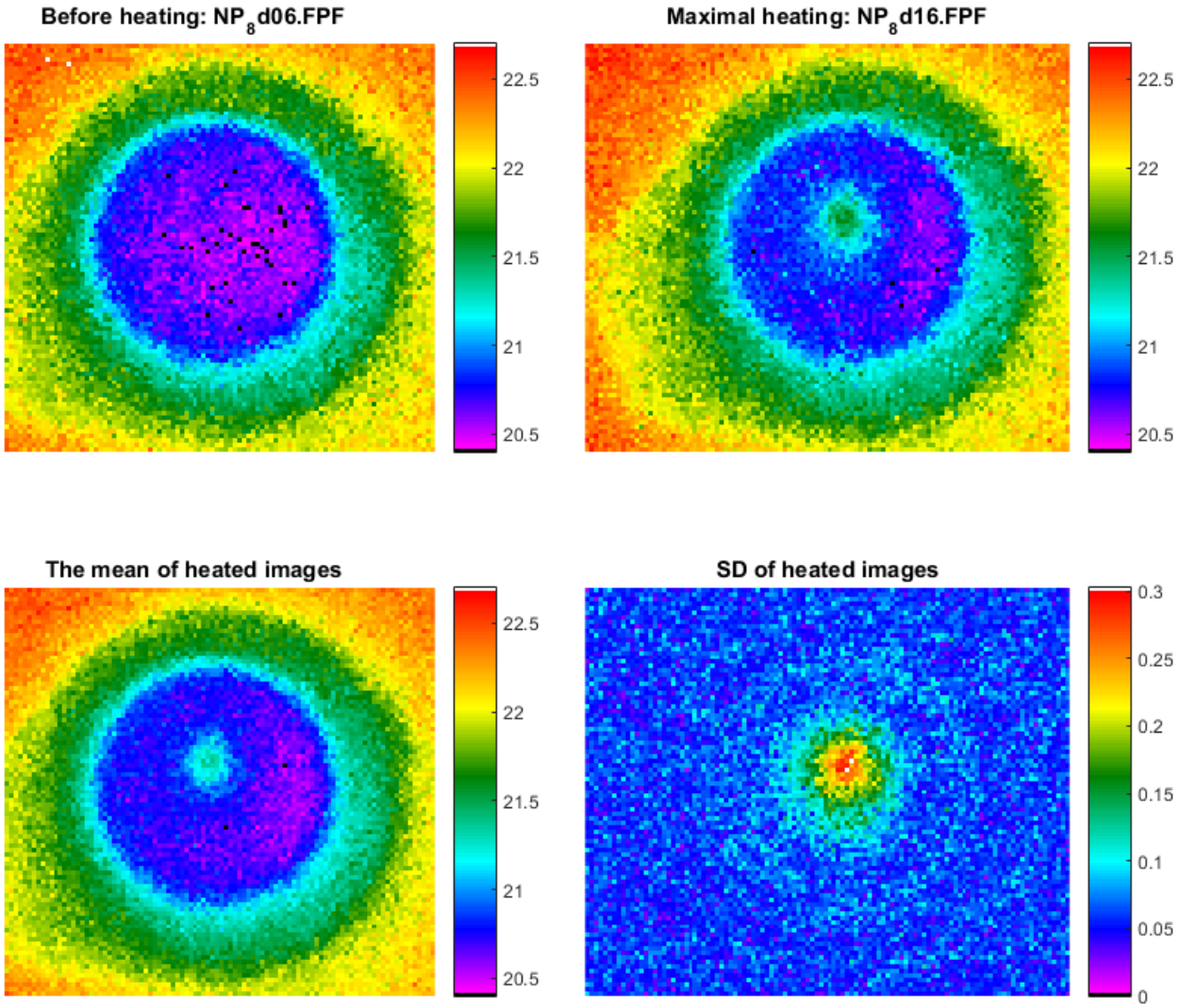


Fig. 3.3.2. Upper panels: the images taken at the start and the end of the illumination. Lower panels: the distributions of the mean temperature and its SD of the hydrosol surface during laser illumination.

Therefore, the preliminary location of the beam center was estimated as the gravity center of the most heated area, which was determined by manual thresholding of the SD image.

The program presents an image only with the points, which SDs are higher than the selected threshold. It gives to a user the option to change the SD threshold in order to clean the image from

points that aren't of interest, that means outside the laser beam. After the threshold $T_h$ selection, a binary hot area mask $M_h$ could be generated. The mask consists of binary mask defines a region of interest (ROI) of the original image. Mask pixel values of unit indicate the image pixel belongs to the ROI. Mask pixel values of zero indicate the image pixel is part of the background. The mask size must be the same as the image being analyzed.

A second stage is the cleaning of the image from those points that have few connected components.

Figure 3.3.3 presents the SD image, on which the SD values higher than the selected threshold are shown in color. The left panel shows all pixels with SD more than 0.217. The right panel shows the left panel image, from which are remove all connected components that have fewer than 16 pixels. The gravity center of the pixels shown in the right panel has coordinates $c_x$ = 58 and $c_y$ = 40, which were supposed to be the preliminary laser beam center.

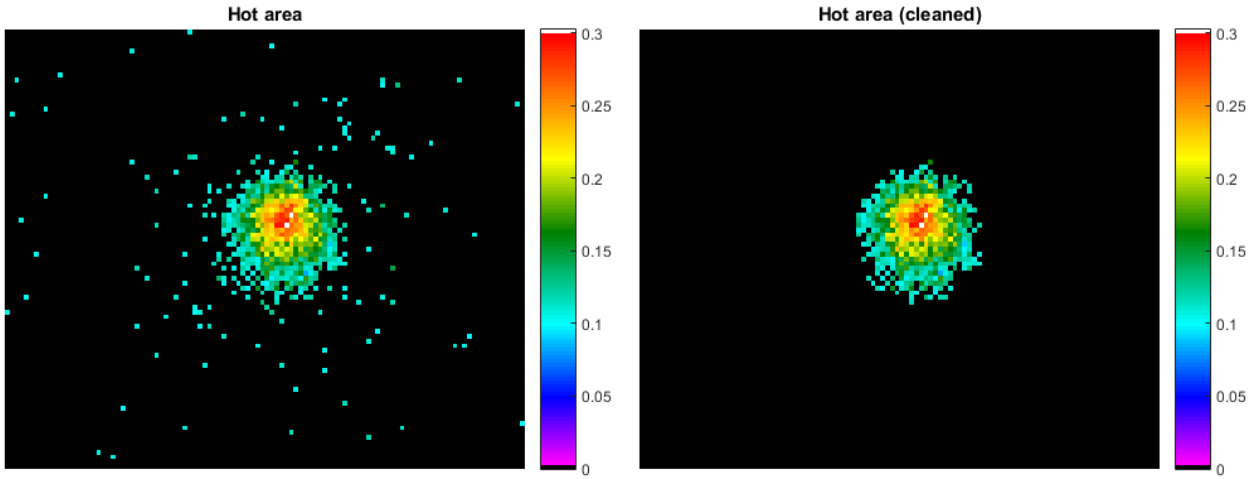


Fig. 3.3.3. The distributions of the SD of the temperature variation of the hydrosol surface during laser illumination. Left: the color points correspond to the SD values between 0.217 and 0.302. Right: the left panel image, from which are remove all connected components that have fewer than 16 pixels.

It is possible to improve the accuracy of the location of the laser beam center by taking into account the axial symmetry of the laser beam and, as result the axial symmetry of the temperature distribution respect to the center. This means that any annulus centered at correct location of the beam center should have minimal temperature variation over the ring in comparison with other

rings. The direct calculation over the annulus of 6 and 7 pixels internal and external radii, respectively, located near the preliminary found center has shown the minimal temperature variation exhibits the annulus located at the point with coordinates $c_x = 58$ and $c_y = 38$. This point will be considered as the refined location of the laser beam center.

Figure 3.3.4. shows the IR image taken at the end of the illumination (maximal heating), on which the the black points (asterisks) on the heated area indicates the preliminary (left panel) and refined (right panel) location of the laser beam. It was found taking into account the distance between the IR camera and hydrosol surface, the field of view and resolution of the camera that a pixel size for the IR images under the study is of 0.21 x 0.21 $mm^2$. The diameter of the laser beam is 3 mm, therefore the beam radius is about 7 pixels. The black line is the circle of seven pixels radius that limits the area illuminated by the laser beam.

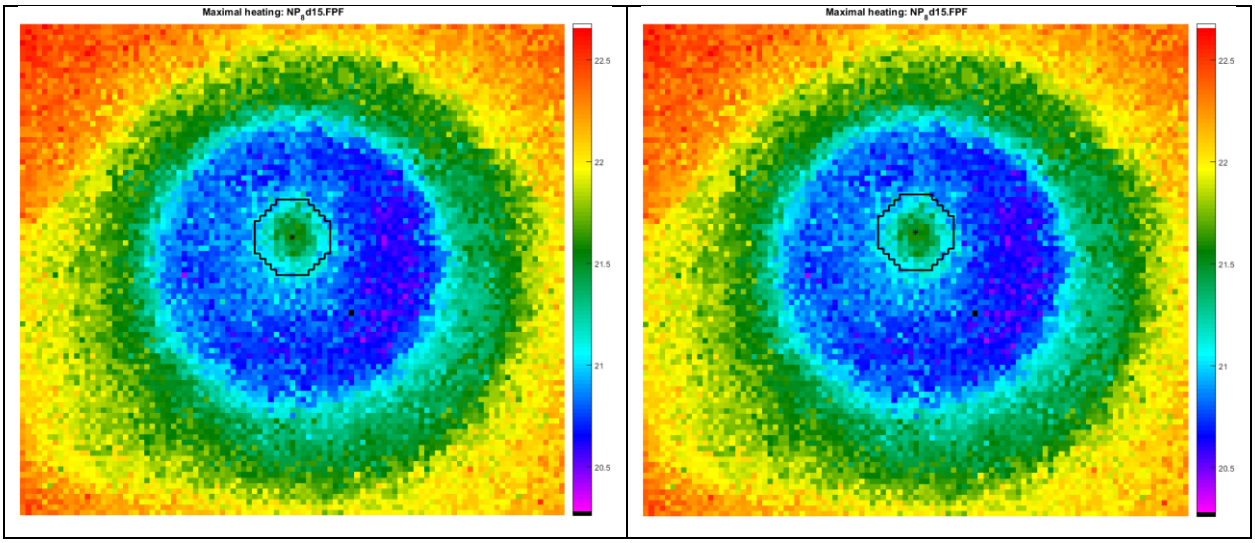


Fig. 3.3.4. The IR image taken at the end of the illumination (maximal heating). The black point (asterisk) on the heated area indicates the estimated location of the laser beam. The black line is the circle of seven pixels radius. Left: the preliminary beam center is found as the gravity center of the pixels shown in the right panel of Figure 3.3.3. Right: the refined beam center is tuned by using the axial symmetry of the temperature distribution.

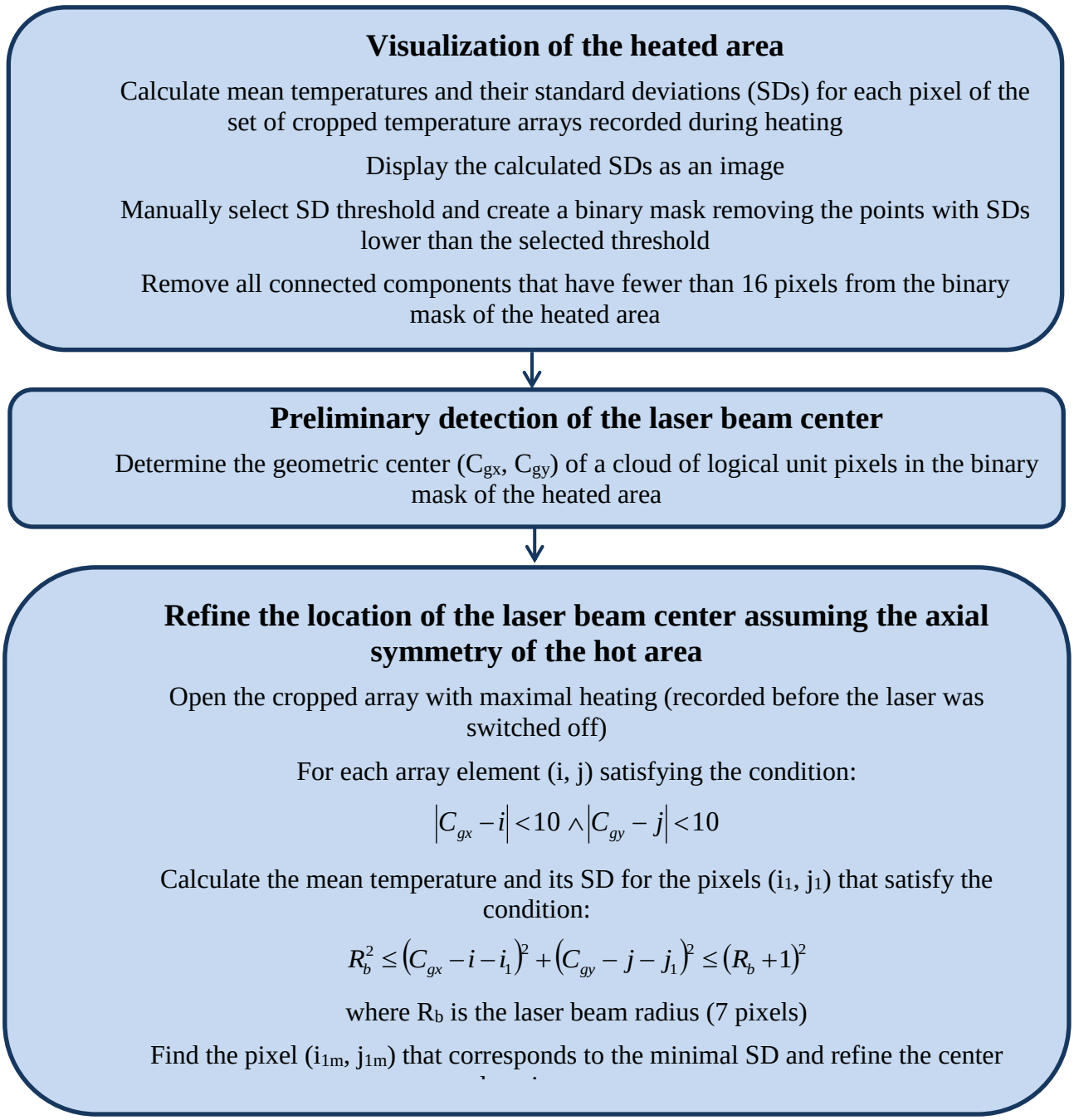


Fig. 3.3.5 Flowchart of MatLab program. The flowchart shows the sequence of steps the data is submitted for analysis to found the center of laser beam.

### 3.3.3 Radial Temperature Distributions over a Hydrosol Surface

Once the center of the region of interest is determined, an evaluation of the temperature distribution over the heated area can be done. The sequence of steps used for the evaluation of the radial temperature distributions (RTDs) is presented in the flowchart in Figure 3.3.2.

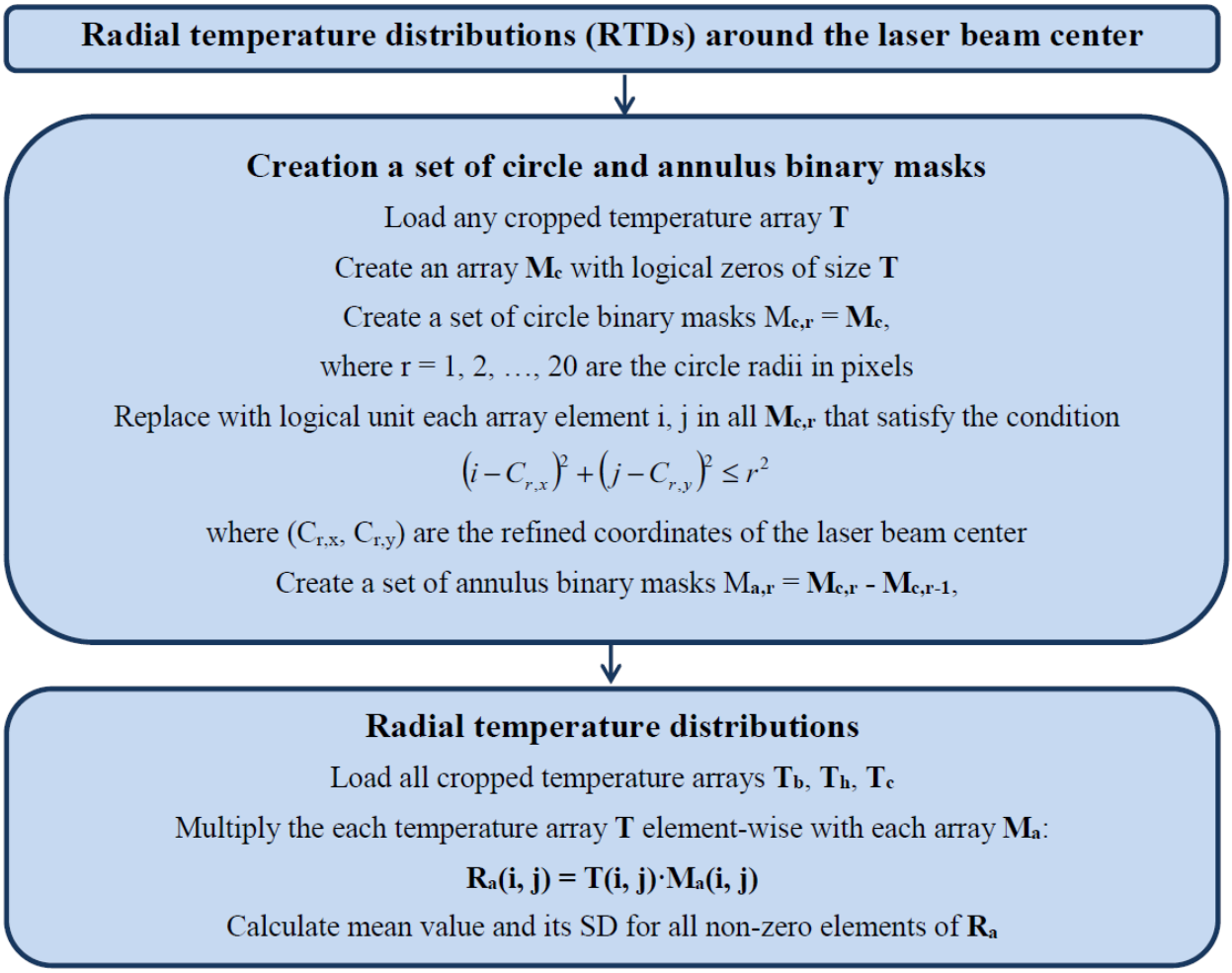


Fig 3.3.6. Flowchart for the evaluation of the radial temperature distributions.

To evaluate the RTDs, a set of circle binary masks was created. The binary mask defines a region of interest (ROI) of the original image. Mask pixel values of unit indicate the image pixel belongs to the ROI. Mask pixel values of zero indicate the image pixel is part of the background. The mask size must be the same as the image being analyzed.

Two simple steps are needed to create the circle masks $M_{c,n}$. On the first step, a logical array of zeros is created. Then, the pixels i, j that are satisfied to the condition

$$(i-c_x)^2+(j-c_y)^2 \le n^2, \qquad (3.3.3)$$

are replaced with units. Here n is the mask number, which corresponds to the circle with the radius of n pixels.

To calculate a RTD around the laser beam center for each IR image, the annulus masks $M_{r,n} = M_{c,n} - M_{c,n-1}$ were created. Having a set of the annulus masks, the temperature distribution over an annulus of given radii and one pixel width centered at $c_x$, $c_y$ can be found.

The left panel of Figure 3.3.6 shows the annulus masks $M_{r,3}$, $M_{r,9}$ and $M_{r,13}$ (crosses) for the image taken at the end of the laser illumination. The selected area is of 33 x 33 pixels and includes the laser-heated area and its vicinity. The asterisk indicates the laser beam center estimated and tuned with the procedure described in the previous subchapter.

The right panel of Figure 3.3.6 present the temperature variations across the annuluses marked on the left panel as a function of the angles (measured clockwise) between the vertical direction and the direction from the laser bean center to a current annulus pixel. The solid lines show mean temperatures over the annuluses while the dashed lines are ± one SD from the means.

The mean temperatures and their SDs for an annulus with the external radius of n pixels selected on the IR image taken at time $t_k$ are defined as

$$T_{meam}(t_k,n)=\frac{1}{N_n}\sum_{i,j}^{N_n}T(t_k,i,j), \qquad (3.3.4)$$

$$T_{SD}(t_k,n)=\sqrt{\frac{1}{N_n-1}\sum_{k=1}^{N_n}\left[T(t_k,i,j)-T_{mean}(t_k,n)\right]^2}, \qquad (3.3.5)$$

where i and j are the pixels satisfying to the condition

$$(n-1)^2 \le (i-c_x)^2+(j-c_y)^2 < n^2 \qquad (3.3.6)$$

and $N_n$ is total number of the pixels satisfying to the condition (3.3.6).

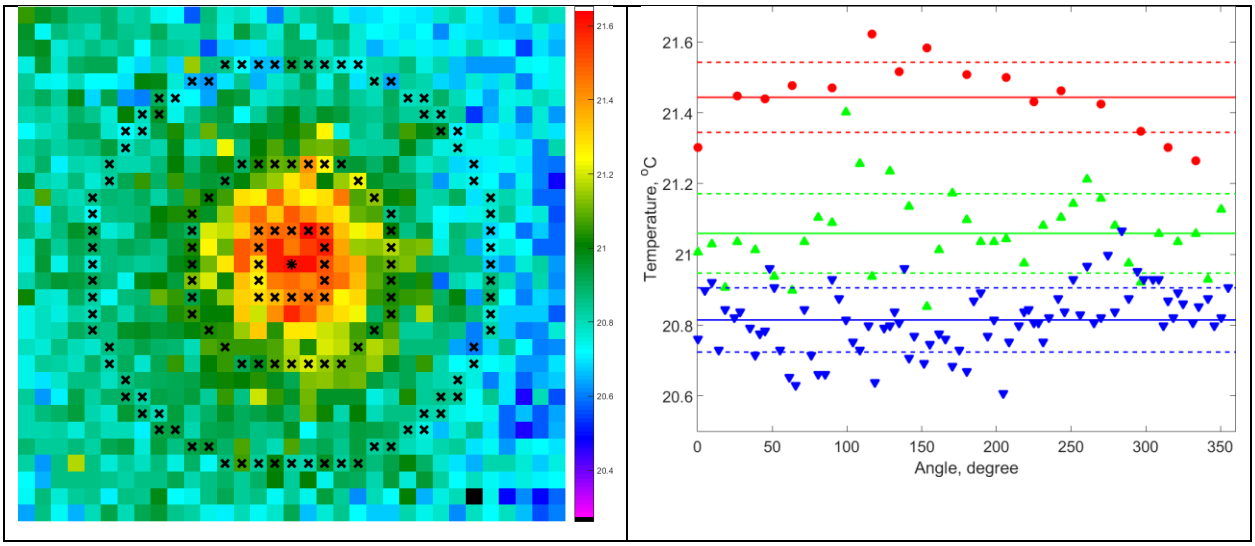


Fig. 3.3.6. Left: the laser heated area and its vicinity (33 x 33 pixels) for the images taken taken at the end of the laser illumination (maximal heating). The asterisk indicates the laser beam center. The crosses mark the pixels, for which the distances from the center are of about 3, 7 and 13 pixels (the annulus masks $M_{r,3}$, $M_{r,9}$ and $M_{r,13}$). Right: the temperature variations across the annuluses marked on the left panel as a function of the angles (see text). The solid lines show mean temperatures over the annuluses while the dashed lines are ± one SDs from the means. The mean values and their SDs are equal to 21.44 ± 0.10, 21.06 ± 0.11 and 20.81 ± 0.09, for the annuluses with the external radii of about 3, 7 and 13 pixels, respectively.

As it is possible to see from right panel of Figure 3.3.6, the standard deviations of $T_{mean}$ are of about 0.1 ºC that could be considered as the error in the temperature measurement with FLIR SC655 IR camera. The angular variation of temperature within the annuluses does not exceed their SDs that evidences the radial symmetry of the temperature distribution respect to the laser beam center. Therefore, the temperatures of the annulus pixels are almost the same that allows us to use for the description of the surface temperature distribution the evaluated set of $T_{mean}(t_k,n)$ and their SDs $T_{SD}(t_k,n)$.

### 3.3.4 Temporal Behavior of the Hydrosol Surface Temperature during and after Laser Illumination

As was shown in the previous subchapter, the temperature distribution is radially symmetric around the laser beam center. Therefore, the temperatures of the annulus pixels are almost the same that allows us to use for the description of the surface temperature distribution the evaluated set of $T_{mean}(t_k,n)$ and their SDs $T_{SD}(t_k,n)$. Figure 3.3.7 shows the temperature maps of the hydrosol surface RTDs during and after the laser illumination. The colors of the concentric annuluses of increasing radii represent their mean temperatures (calculated using Eq. 3.3.4) in accordance with the color bar.

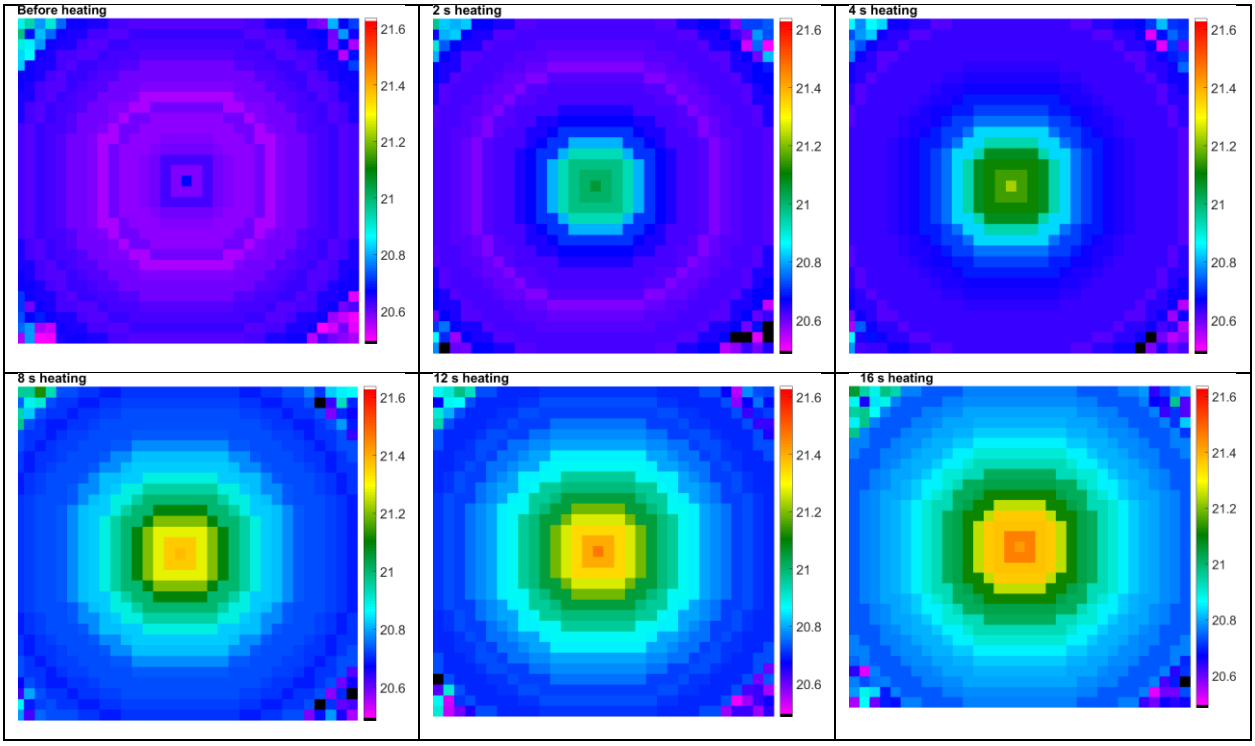

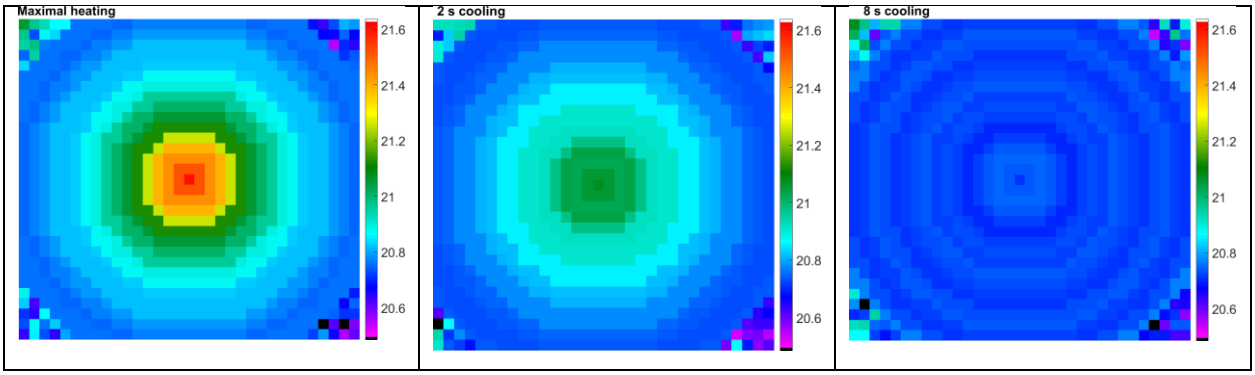


Fig. 3.3.7. Radial temperature distributions of the hydrosol surface evaluated from the corresponding IP images taken at indicated times during heating under the laser illumination and during the subsequent cooling.

The temporal dependences of RTDs at selected distances from the laser beam center are shown in Figure 3.3.8. All dependences exhibit the similar behavior. When the laser being switched on the temperature increases and goes to a saturation temperature. After the switch off the laser, the temperature decreases and returns to the temperature that was before the laser illumination.

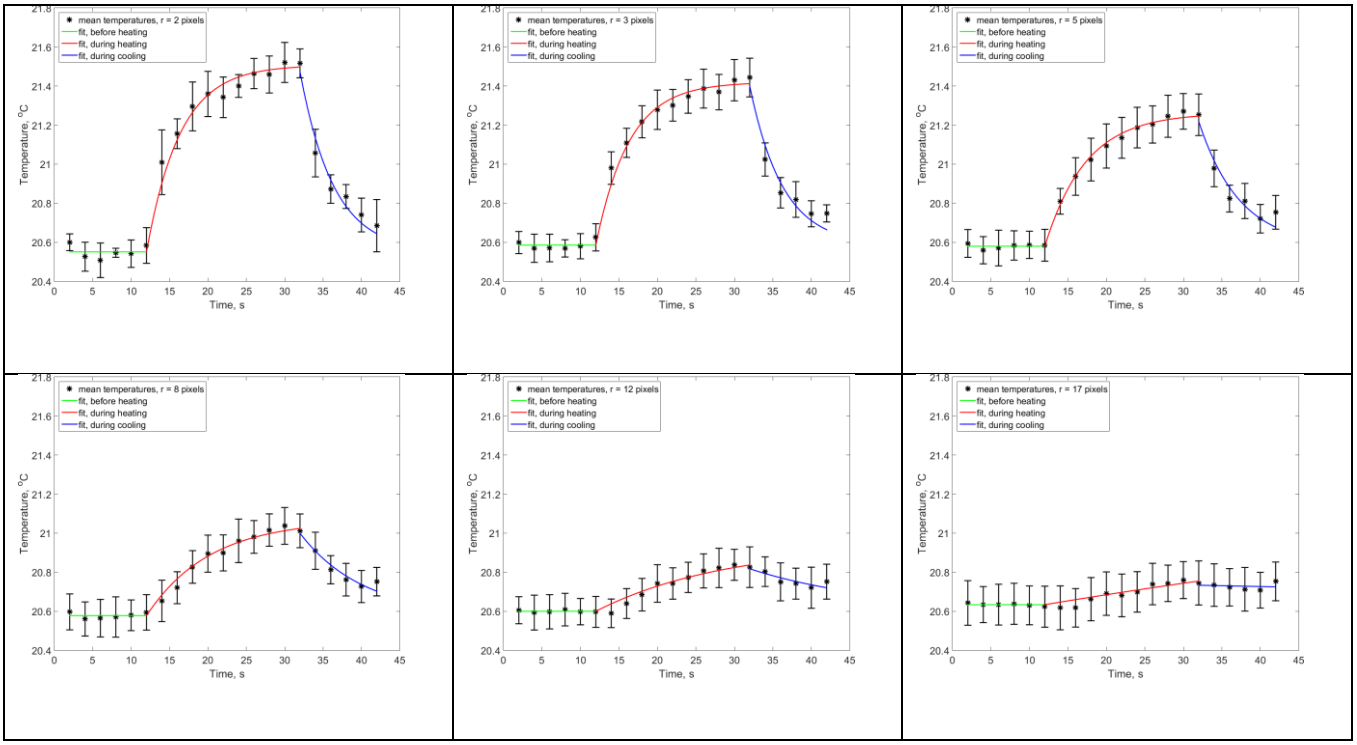

Fig. 3.3.8. Temporal dependences of mean temperatures over the annuluses of indicated radii and one pixel width. The bars indicate the SD of the temperature over the annuluses. The lines are the fitting to Eqs. 3.3.7 and 3.3.8 with the parameters presented in Figure 3.3.9.

A simplified description of the temporal behavior of the RTDs during and after laser illumination can be made using a model proposed in (Richardson et al., 2009). The model employs a heat generation in GNPs illuminated with laser light and its dissipation in water. The heated water are cooled is due to convective heat transfer from hydrosol surface to surrounding air. The temperature increases during laser illumination after a laser being switched on at time $t_{on}$ (heating stage) is described by the formula

$$T(t) = T_m - (T_m - T_0)\exp\left[-B(t - t_{on})\right], \qquad (3.3.7)$$

where $T_0$ is the ambient temperature and $T_m$ is the saturation temperature when t goes to infinity.

After the switching off the laser at time $t_{off}$ (cooling stage), the temperature decreases in accordance with the equation

$$T(t) = T_0 - (T_0 - T_{off})\exp\left[-B(t - t_{off})\right]. \qquad (3.3.8)$$

where the parameter

$$B = \frac{hS}{m_w c_w}, \qquad (3.3.9)$$

is the rate constant of heat loss, S is the surface area and $T_0$ is the ambient temperature, $m_w$ and $c_w$ are the mass and heat capacity of water.

The saturation temperatures is given by the formula

$$T_m = T_0 + \frac{I\left(1 - 10^{-A_\lambda}\right)}{hS}, \qquad (3.3.10)$$

where I is the incident laser power, $A_\lambda$ is the absorbance of the hydrosol, h is a heat transfer coefficient between water and air.

The presented above model was used to describe the experimental temporal dependences. For this, the model parameters, such as B, $T_0$, $T_{off}$ and $T_m$ were found by fitting dependences the dependences to Eqs. 3.3.7 and 3.3.8. The fitting was carried out in two steps. In the first, the dependences at the cooling stage were fitted to Eq. 3.3.8 and the parametrs B, $T_0$ and $T_{off}$ were obtained. Then, the dependences at the heating stage were fitted to Eq. 3.3.7 using the values B obtained at the first step and fitting the rest unknown parameter $T_m$. The evaluated parameters are

shown in Figure 3.3.9. The parameter $T_0$ is almost the same for all dependences and closed to the temperature outside the laser beam. The parameters $T_m$ and $T_{off}$ are maximal at the beam centers and decrease when the radius increases. At radius less than 4 pixels $T_m$ and $T_{off}$ are the same due to saturation of the heating process, which is achieved when the rate of energy absorption is equal to the rate of heat loss. The incomplete saturation of the heating process on the periphery and outside the laser beam (radius of the beam is of 7 pixels) causes the difference between $T_m$ and $T_{off}$ which increases with the radius increasing. The parameter B is about of 0.23 1/s at the beam centers and decreases with the radius increasing.

The results of fitting are represents by solid lines in Figure 3.3.8. It is possible to see that all experimental temporal dependences are fitted well that evidences the possibility to use Eqs. 3.3.7 and and 3.3.8 for description of the temporal behavior of the hydrosol surface temperature during and after laser illumination. From the other hand, it is important to underline that the used simple model was developed for a small drop filled with a hydrosol and cannot describe the temperature behavior in our case. Therefore, the fitted curves as well as the fitted parameters should be considered only as a phenomenological description.

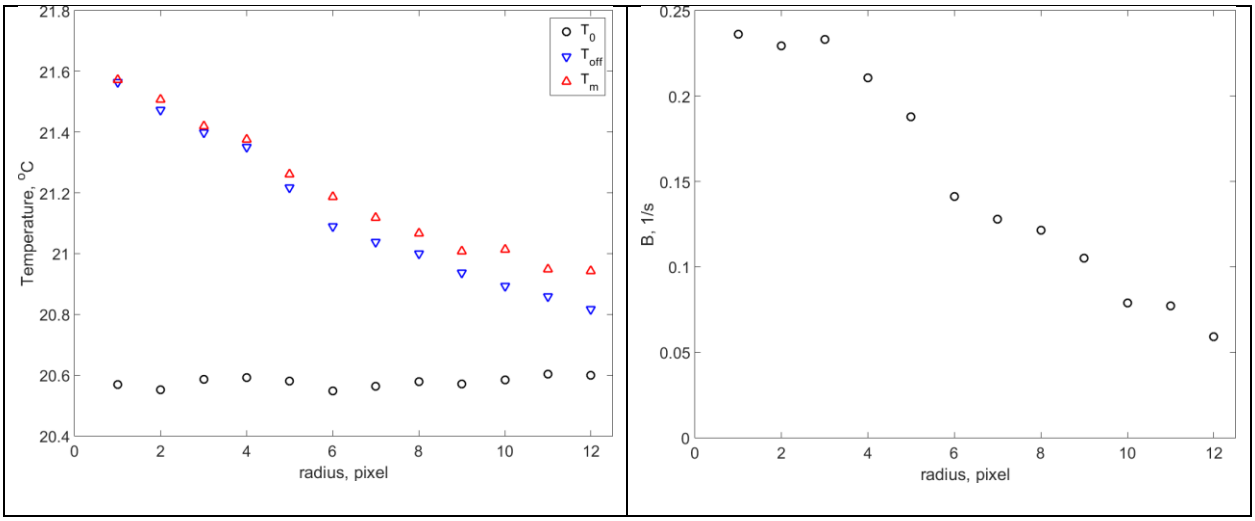


Fig. 3.3.9. Dependences of fitted parameters $T_0$, $T_{off}$ and $T_m$ (left) and B (right) on the annulus radius.

# CHAPTER 4

# THEORETICAL STUDIES ON THE PHOTOTHERMAL EFFECT IN GOLD HYDROSOL

In this chapter, a theoretical analysis of the radial temperature distributions in the gold hydrosol under illumination with a laser light will be presented. The analysis will be based on the numerical calculations performed with the finite-elements software COMSOL Multiphysics. The first subsection describes the basic equation for the two-dimensional case within the semi-infinity space, material properties and adjusted parameters used for the simulations. The influence of the parameters on the calculated temperature fields and their adjustment ensuring the maximum coincidence between the calculated and experimental temperature distributions will be presented in the second subchapter. In the third subsection, phenomenological equations relating the volume temperature distributions to the surface ones will be proposed.

## 4.1 Base Equations and Parameters Used for Calculations

### 4.1.1 Heating stage

Consider an isotropic homogeneous semi-infinite hydrosol, whose surface is illuminated by a laser beam of given radius $R_b$ falling perpendicular to the surface. Additionally, we will suppose that incident light is absorbed by the hydrosol and produces the heat at the rate per unit time per unit volume , Qin et al., (2012)

$$Q(z) = n_{GNP}\sigma_a I(z), \qquad (4.1.1)$$

where $n_{GNP}$ is the GNP concentration, $\sigma_a$ is the absorption cross-section and I(z) is the local laser fluence at distance z from the hydrosol surface.

The attenuation of the laser beam is described by the Beer–Lambert law

$$I(z) = I_0 10^{-A} = I_0 \exp\left(-n_{GNP}\sigma_{ex} z\right) = I_0 \exp\left(-\frac{z}{a}\right), \qquad (4.1.2)$$

where $I_0$ is the incident laser fluence at the hydrosol surface, A is the absorbance of the hydrosol with the thickness z, $\sigma_{ex} = \sigma_a/f_a$ is the extinction cross section, $f_a$ = is the relative absorption efficiency of the hydrosol (a measure of how much of the nontransmitted light is absorbed rather

than scattered) and a = $f_a/n_{GNP}\sigma_a$ is the light attenuation length, at which the light intensity is attenuated by e times.

The relative absorption efficiency $f_a$ is named as the theoretical conversion efficiency of a single NP , according to Qin et al., (2012), a measure of how much of the nontransmitted light is absorbed rather than scattered. As was mentioned in the subchapter 3.1.2 $f_a$ is closed to unity and was considered equal to 0.9. From the other hand, the measured photothermal conversion efficiency $f_m$ is a bulk property that depends not only on the NP, but also on radiative transport and environmental factors (e.g. measurement setup), while the theoretical efficiency is dependent only on the NP, predicted by Maxwell's equation ; Qin et al., (2012).

We will suppose that the laser beam is near-uniform within a circular disk (top-hat beam), therefore the incident laser fluence can be written as

$$I_0(r) = \frac{P_0}{\pi R_b^2}\left[H(r) - H(r - R_b)\right], \qquad (4.1.3)$$

where $P_0$ is the laser optical power, which is a constant for a continuous-wave laser. The function H(r) is the Heaviside step function, which is equal to zero at r < 0 and to one at r > 0.

Combining (4.1.1), (4.1.2) and (4.1.3), and introducing measured photothermal conversion efficiency $f_m$ we can present the local heating rate as

$$Q(r,z) = Q_0 f_m\left[H(r) - H(r - R_b)\right]\exp\left(-\frac{z}{a}\right), \qquad (4.1.4)$$

where

$$Q_0(r) = \frac{P_0 n_{GNP}\sigma_a f_m}{\pi R_b^2} \qquad (4.1.5)$$

is the theoretical heating rate at the hydrosol surface at the laser illuminated area.

Taking into account the cylindrical symmetry respect to the beam axis, the transient heat conduction equation can be written as (Yilbas et al., 2013, p. 13):

$$c_w\rho_w \frac{\partial T_h(r,z,t)}{\partial t} = k_w\left\{\frac{1}{r}\frac{\partial}{\partial r}\left[r\frac{\partial T_h(r,z,t)}{\partial r}\right] + \frac{\partial^2 T_h(r,z,t)}{\partial z^2}\right\} + Q(r,z) \qquad (4.1.6)$$

Here $T_h(r,z,t)$ is the temperature distribution within the semi-infinity hydrosol during heating, r is the radial direction (normal to the laser beam axis), x is the axial direction (along the

laser beam axis). The parameters $c_w$, $\rho_m$ and $k_m$ are the specific heat, the density and the thermal conductivity of the hydrosol, respectively, which we will assume to be equal to those of pure water.

The heat supplied by absorption of NPs in the hydrogel is dissipated by transfer through the hydrogel surface to a surrounding media (air), which is kept at constant temperature $T_0$. At temperatures closed to room temperature, the only convective heat transfer is significant. Therefore, the rate of energy flowing out of the hydrogel will be proportional to the temperature difference, $T_h(t,0) - T_0$, between the hydrogel and its surrounding with the coefficient of proportionality h called as the heat transfer coefficient.

Equating the heat fluxes at the one side of the boundaries with their equivalents at the other side, we can write the boundary condition at z = 0 as:

$$k_w \left.\frac{\partial T_h(r,z,t)}{\partial z}\right|_{z=0} = h\left[T_h(r,0,t) - T_0\right], \qquad (4.1.7)$$

We will assume that before starting the illumination the hydrosol is kept at uniform temperature that is equal to those of surrounding air, therefore the initial condition is

$$T_h(r,z,0) = 0, \qquad (4.1.8)$$

### 4.1.2 Cooling stage

After switching off the illumination at time $t_{off}$ the local heating rate is equal to zero and the transient heat conduction equation (4.1.6) is reduced to

$$c_w \rho_w \frac{\partial T_c(r,z,t)}{\partial t} = k_w \left\{ \frac{1}{r}\frac{\partial}{\partial r}\left[ r \frac{\partial T_c(r,z,t)}{\partial r} \right] + \frac{\partial^2 T_c(r,z,t)}{\partial z^2} \right\} \qquad (4.1.9)$$

where $T_c(r,z,t)$ is the temperature distribution within the semi-infinity hydrosol during cooling.

The boundary condition is the same as for the heating stage:

$$k_w \left.\frac{\partial T_c(r,z,t)}{\partial z}\right|_{z=0} = h\left[T_c(r,0,t) - T_0\right], \qquad (4.1.10)$$

while the initial condition should be rewritten as

$$T_c(r,z,0) = T_h(r,z,t_{off}), \qquad (4.1.11)$$

where $T_h(r,z,t_{off})$ is the temperature distribution in the hydrosol at the end of the laser illumination.

### 4.1.3 Parameters related to the light-to-heat conversion

As follows from the base equations describing the heat transfer in the hydrosol illuminated with light, there are two groups of parameters needed for theoretical study on the photothermal effect in the hydrosol. The first group are the parameters that describe to the light-to-heat conversion in individual NPs. The list of these parameters, their symbols and values as well as the description of their evaluation method are presented in Table 4.1. The second group includes the parameters related to the heat transfer in the hydrosol, which we will assume to be equal to those of pure water. These parameters are presented in Table 4.2.

Table 4.1 Parameters related to the light-to-heat conversion in individual NPs.

| **Parameter** | **Symbol** | **Value** | **Evaluation method** |
|---|---|---|---|
| GNP concentration | $n_{GNP}$, $m^{-3}$ | $1.70\times10^{18}$ | Estimated in Ch. 3.1.2 |
| Extinction cross section of the GNP for the laser laser stimulation light of 632 nm | $\sigma_{ex}$, $m^{-2}$ | $3.44\times10^{-16}$ | Estimated in Ch. 3.1.2 |
| Relative absorption efficiency of the GNP | $f_a$ | $0.90\times10^{-1}$ | Prevo et al., 2008 |
| Absorption cross section of the GNP | $\sigma_a$, $m^{-2}$ | $3.10\times10^{-16}$ | Calculated as $\sigma_a = f_a\sigma_{ex}$ |
| Light attenuation length | a, $m^{-1}$ | $1.70\times10^{-3}$ | Calculated as $a = 1/n_{GNP}\sigma_{ex}$ |
| Laser optical power | $P_0$, W | $3.00\times10^{-2}$ | In correspondence with the experiment |
| Laser beam radius | $R_b$, m | $1.50\times10^{-3}$ | In correspondence with the experiment |
| Heating rate at the hydrosol surface | $Q_0$, $W\cdot m^{-3}$ | $2.29\times10^{6}$ | Calculated with eq. (4.1.5) |

Table 4.2 Parameters related to the heat transfer in water.

| **Parameter** | **Symbol** | **Value** | **Evaluation method** |
|---|---|---|---|
| Heat capacity at constant pressure | $c_w$, $J\cdot kg^{-1}\cdot K^{-1}$ | $4.18\times10^{3}$ | COMSOL value at 300 K |
| Density | $\rho_w$, $kg^{1}\cdot m^{-3}$ | $1.00\times10^{3}$ | COMSOL value at 300 K |

| | | | |
|---|---|---|---|
| Thermal conductivity | $k_m$, $W \cdot m^{-1} \cdot K^{-1}$ | $0.60 \times 10^{-1}$ | COMSOL value at 300 K |
| Heat transfer coefficient. | h, $W \cdot m^{-2} \cdot K^{-1}$ | 1100 | Adjusted in Ch. 4.3.2 |

In our experiment the dominant material is water, so the properties values used in the simulations are those of such material. COMSOL Multiphysics use an expression dependent on the temperature for the value of material properties, so instead of a constant a range of values are used for the material properties.

For this simulation there are only 3 material properties needed to solve the heat transfer equation, $c_w$, $\rho_m$ and $k_m$ (water density, heat capacity and thermal conductivity respectively). According to our experimental results, we are working in a range between 293.65K and 294.75K. We can obtain the material properties from the following tables.

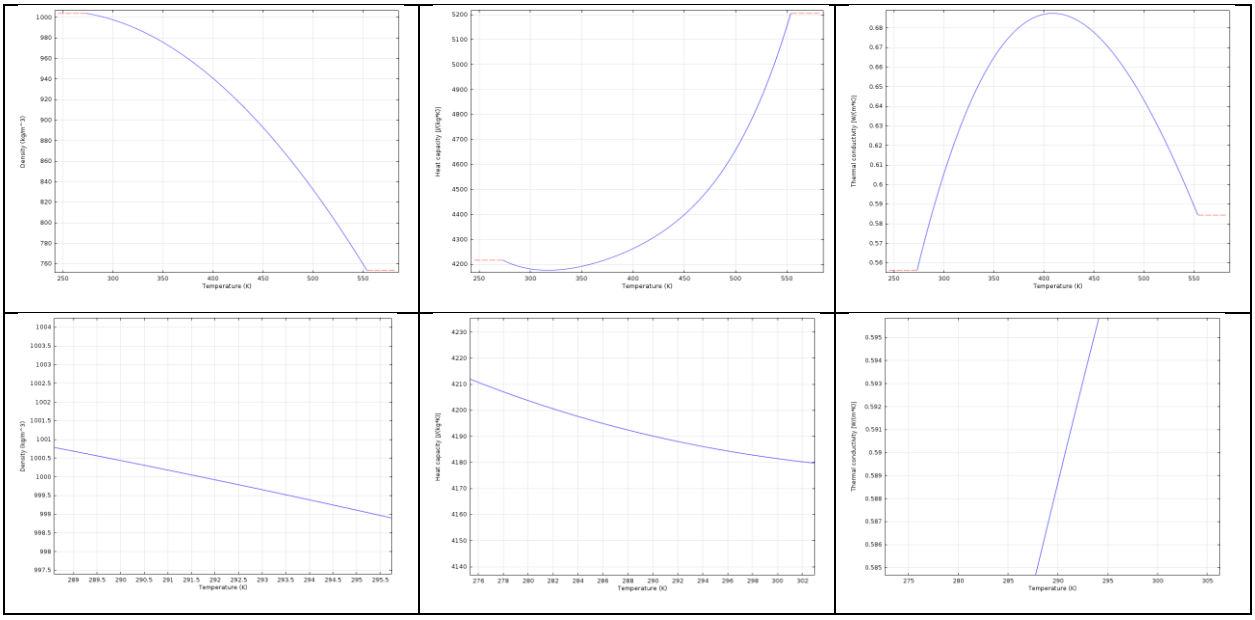

Fig 4.1.1. Plot values for density of water, heat capacity and thermal conductivity respectively at a wide range of temperatures (top) and bottom plots show the same parameter at our range of interest for temperature. It is clear that for our temperature this parameter are quasi constants.

## 4.2 Finite-element Modelling of Heating and Cooling the Hydrosol by Laser Light

### 4.2.1 Temperature Distributions for Different Adjusted Parameters

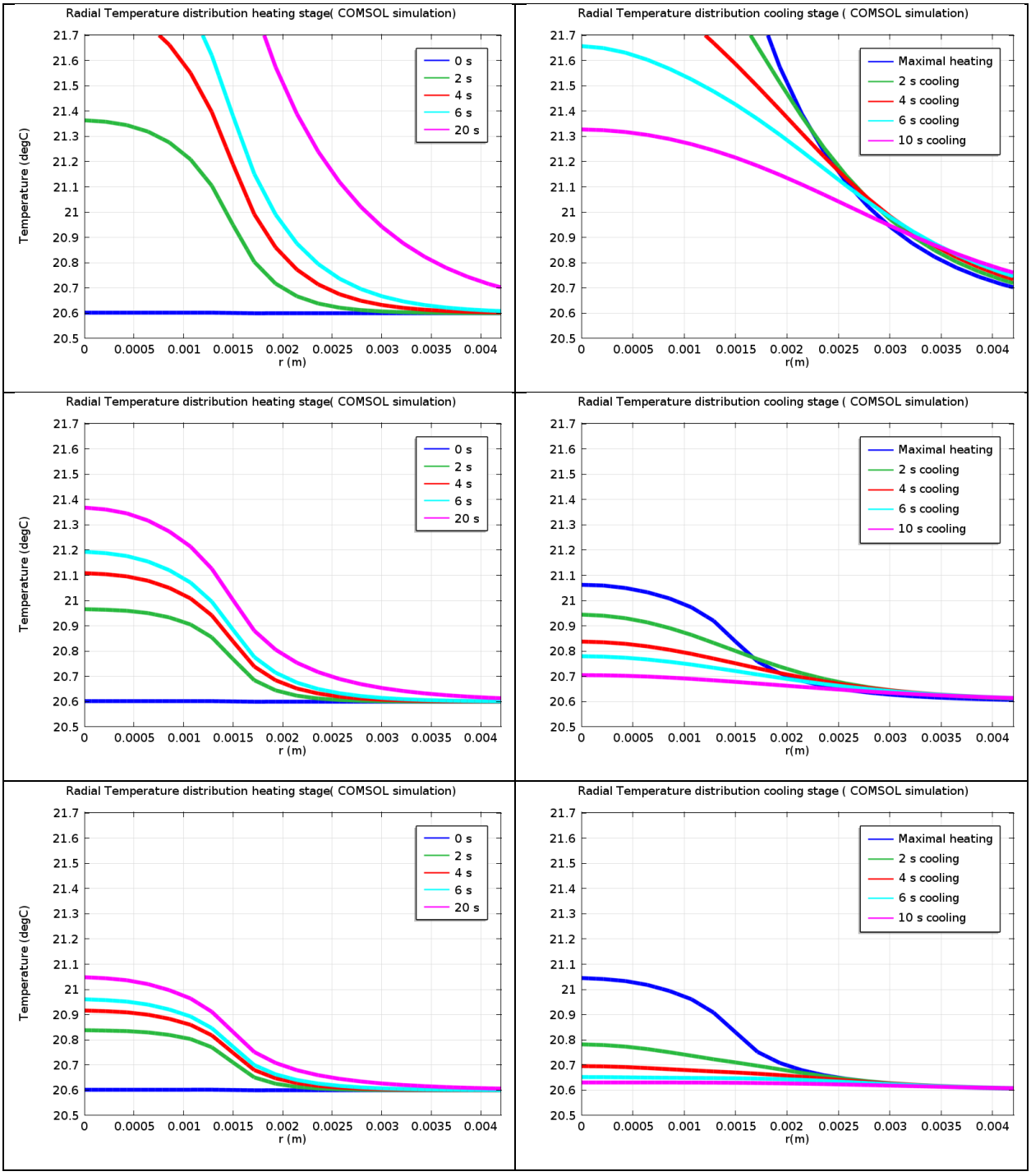

Fig. 4.2.1 Top row shows COMSOL simulations for heat transfer coefficient h=50. Middle rows h=1525 and bottom rows the constant is h=3000.

From previous figure it can be conclude that if the value of h increases the temperature decreases. From the first column it is also clear that the value of parameter h affects principally the surfaces' temperature.

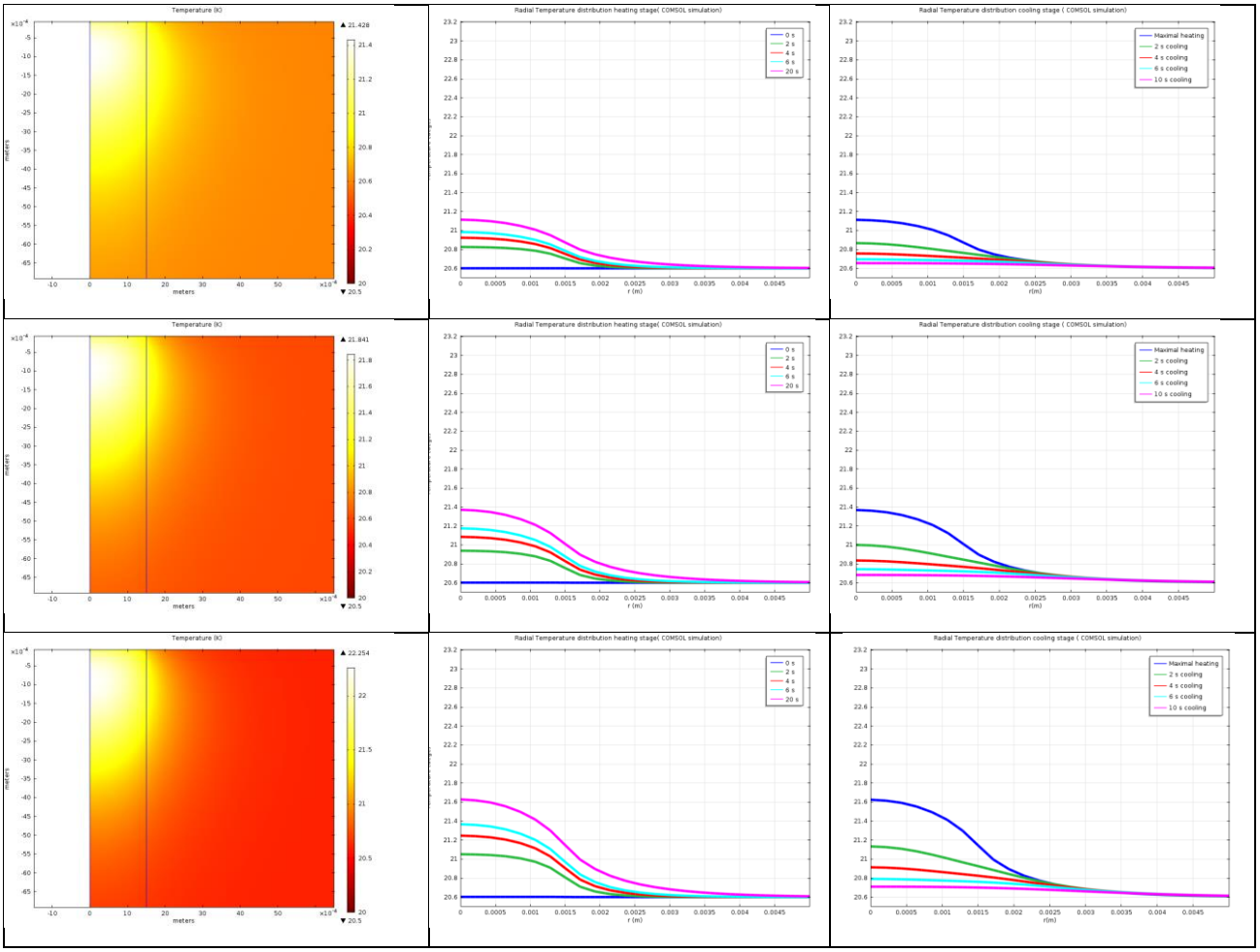


Fig. 4.2.2 Figure shows variation of the parameter $Q_0$. Top row shows a value for $Q_0$ of 50% of original value while middle and bottom row shows the simulation with 75% and 100% of $Q_0$ total reported on table 4.1.

Figure 4.2.2 shows evidence that if the value of the parameter Q0 is directly related with temperature, the higher value of Q0 the higher temperature increases specially the volumetric temperature.

## 4.3 The Adjustment of the Heat Transfer Coefficient and Estimation of the Photothermal Conversion Efficiency

### 4.3.1 COMSOL Analogues of the Measured Radial Temperature Distributions

To compare the results of numerical COMSOL simulation with the surface RTDs evaluated in Ch. 3 it is necessary to take into account that the measured RTDs represent the mean temperatures over annuluses of finite thickness.

The exact mean temperature over an annulus with radii ri and ri - Δr with the temperature distribution T(r) is equal to

$$T_{mean}(r_i) = \frac{2\pi}{\pi r_i^2 - \pi(r_i - \Delta r)^2} \int_{r_i-\Delta r}^{r_i} T(r) r dr = \frac{2}{\Delta r(2r_i - \Delta r)} \int_{r_i-\Delta r}^{r_i} T(r) r dr \qquad (4.3.1)$$

For our purpose, it is enough to suppose the linear temperature change over the ring:

$$T(r) = T(r_i - \Delta r) + \frac{T(r_i) - T(r_i - \Delta r)}{\Delta r}(r - r_i + \Delta r) \qquad (4.3.2)$$

that gives

$$T_{mean}(r_i) = \frac{T(r_i - \Delta r)(3r_i - 2\Delta r) + T(r_i)(3r_i - \Delta r)}{3(2r_i - \Delta r)} . \qquad (4.3.3)$$

Substituting ri with ilpix and Δr with lpix in (4.3.4) we will have the COMSOL analogues of RTDs:

$$R_{cal}(r_i, t_j, h) = \frac{T(r_i - l_{pix}, t_j, h)(3i - 2) + T(r_i, t_j, h)(3i - 1)}{3(2i - 1)} , \qquad (4.3.4)$$

where T(r, t, h) is the surface temperature at distance r from the laser beam center and time t calculated with the COMSOL Multiphysics.

The comparison of the temperature distributions T(r, t) calculated with the COMSOL Multiphysics (lines) and their RTD analogues s evaluated with Eq. 4.3.5 (circles) for the heating

and cooling stages are shown in Figure 4.3.1. The calculations were made with the parameters presented in Tables 4.1.1 and 4.1.2. The temperature distributions and RTDs are closed each to others, but are not coincide fully. The most noticeable difference corresponds to the maximal temperature change.

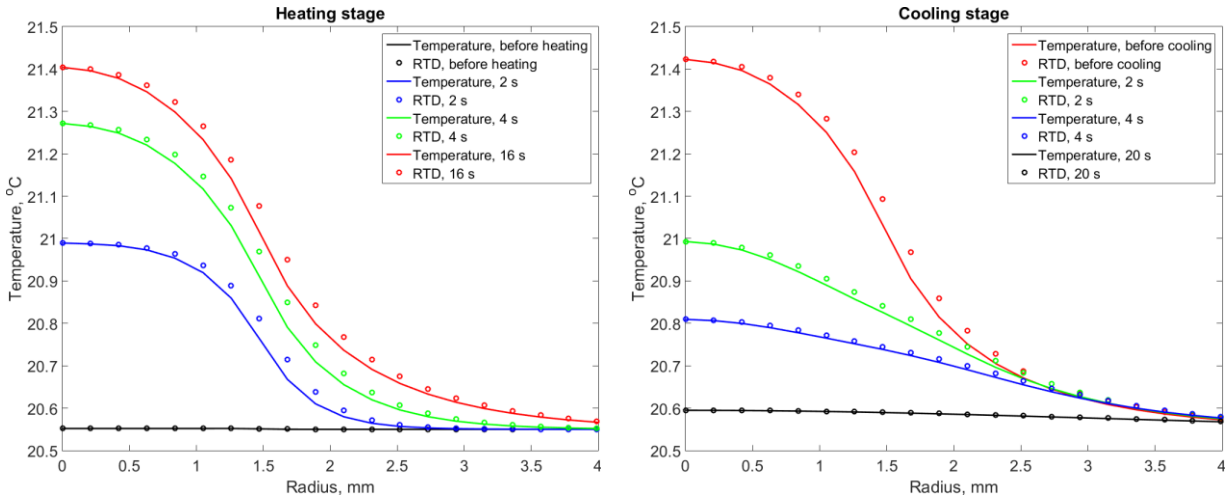


Fig 4.3.1 Temperature distributions T(r, t) calculated with the COMSOL Multiphysics (lines) and corresponding RTDs evaluated with Eq. 4.3.5 (circles) for the heating (right) and cooling (left) stages at the indicated times.

### 4.3.2 Adjustment of the Heat Transfer Coefficient

To provide numerical simulations with the COMSOL Multiphysics Heat Transfer module it is necessary to set up the material properties of the media under the study that in the case of gold hydrosol is water. There are only four parameters (see table 4.1.2) that are needed to perform the simulations. Three of them, the specific heat, the density and the thermal conductivity of water are well established and directly given in the module. The fourth parameter, heat transfer coefficient h does not presented in the COMSOL list of water properties and should be specified by a user. Preliminary simulations have shown that the h parameter influences drastically the temperature change in the hydrosol volume and especially on its surface. To overcome this problem, the h parameter was adjusted to give the best fit between simulated and measured surface RTDs. The cooling stage does not depend on the parameters related to the light-to-heat conversion in

individual GNPs and is described with only four material parameter, three of which are well established. Therefore, to adjust the h parameter, the experimental surface RTDs for the images recorded during cooling after the laser being switched off were used.

The adjustment procedure is based on minimizing the objective function

$$\Phi(h) = \frac{1}{n_r n_c} \sum_{i=1}^{n_r} \sum_{j=1}^{n_c} \left[ R_{\exp}\left(r_i, t_j\right) - R_{cal}\left(r_i, t_j, h\right) \right]^2 . \quad (4.3.5)$$

Here Rexp(ri, tj) and Rcal(ri, tj, h) are the evaluated RTDs and their COMSOL analogues (calculated with given h) at the cooling times tj in the annuluses with the external radius and width of ri = ilpix and lpix, respectively. lpix is the distance corresponding to one pixel on the IR images. nr and nc are the maximal radius (in pixel) and number of cooling times considered for the adjustment.

The upper left panel of Figure 4.3.2 presents the objective function (4.3.5) calculated for the fm = 1 and a set of the heat transfer coefficient ranged from 800 to 1500 W·m-2·K-1. The objective function was calculated for the RTDs measured at the end of heating and after 2, 4 and 6 s cooling (nc = 4) and for a set of the annuluses with the external radii from 1 to 5 pixels (nr = 5, r5 = 0.1 mm). The objective function exhibits a global minima located at h closed to 1100 W·m-2·K-1. This value gives the best match between the measured and calculated RTDs for the points with radii less than 0.1 mm (5 pixels) as it can be seen in the right upper panel of Figure 4.3.2, on which the experimental and calculated with COMSOL RTDs are compared. At higher radii, a noticeable discrepancy between the experimental and calculated RTDs is observed. The reason of the discrepancy is not clear and it should be the subject of ongoing study. A possible reason of the discrepancy could be the fact that the laser beam is not the top-hat beam.

The lower left and right panel show the effect of the value h on the coincidence between the the measured and calculated RTDs. It is possible to see the too small (800 W·m-2·K-1) or too large (1500 W·m-2·K-1) values lead to the pronounced difference between the experimental and calculated RTDs.

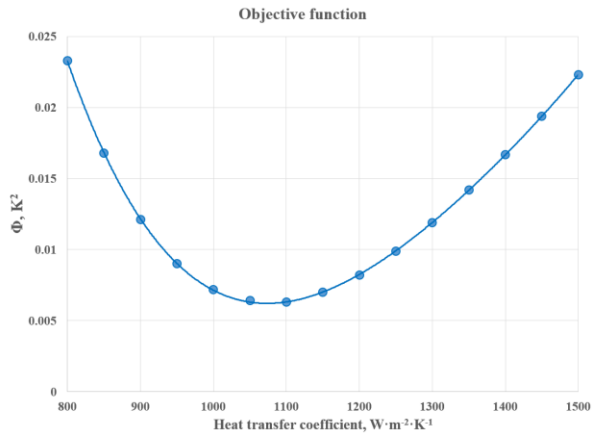
Objective function
Φ, K²
Heat transfer coefficient, W·m⁻²·K⁻¹

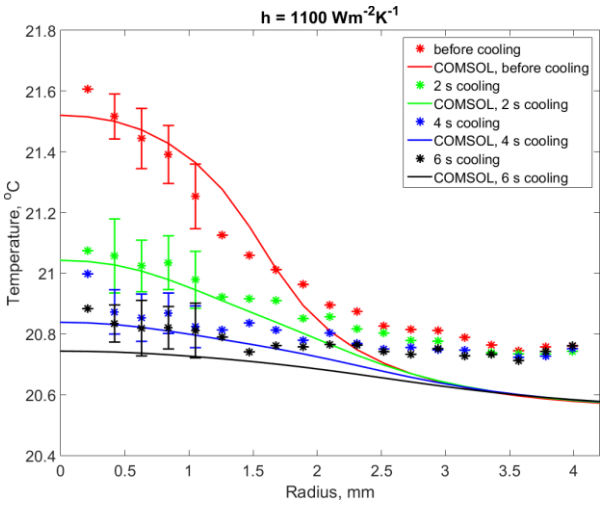
h = 1100 Wm⁻²K⁻¹
before cooling
COMSOL, before cooling
2 s cooling
COMSOL, 2 s cooling
4 s cooling
COMSOL, 4 s cooling
6 s cooling
COMSOL, 6 s cooling
Temperature, °C
Radius, mm

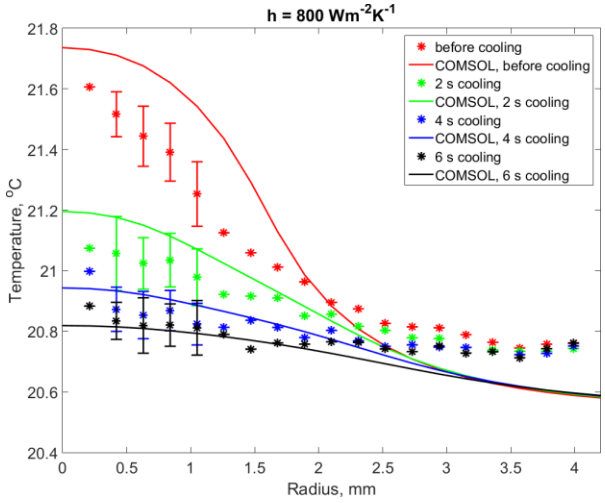
h = 800 Wm⁻²K⁻¹
before cooling
COMSOL, before cooling
2 s cooling
COMSOL, 2 s cooling
4 s cooling
COMSOL, 4 s cooling
6 s cooling
COMSOL, 6 s cooling
Temperature, °C
Radius, mm

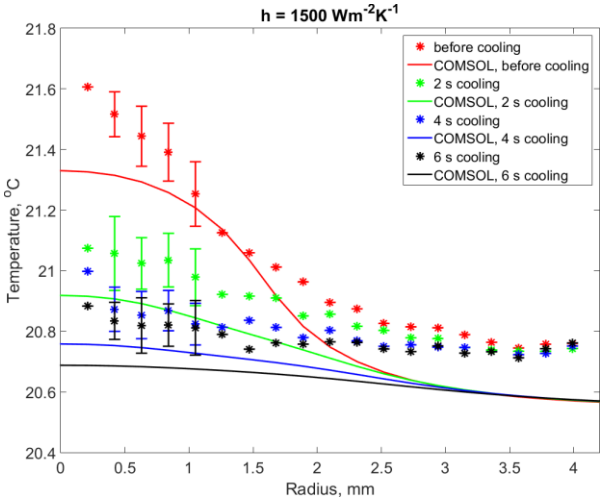
h = 1500 Wm⁻²K⁻¹
before cooling
COMSOL, before cooling
2 s cooling
COMSOL, 2 s cooling
4 s cooling
COMSOL, 4 s cooling
6 s cooling
COMSOL, 6 s cooling
Temperature, °C
Radius, mm

Fig 4.3.2 Upper left: the objective function (4.3.5) as a function of the heat transfer coefficient for the set of the annuluses with the external radii from 1 to 5 pixels (0.21 – 1.05 mm). Upper right, lower left and lower right: comparison of the measured and calculated RTDs for the cooling stage. The measured RTDs (points) and their SDs (error bars(*)) are evaluated with the procedure described in the subchapter 3.3.3. The corresponding COMSOL RTDs (lines) are calculated with Eq. 4.3.4 using the surface temperature distribution found with the COMSOL Multiphysics.

(*) The error bars are shown for the points included in the objective function only, the points at r = 0.21 mm that have SD = 0 were also included in the objective function.

### 4.3.3 Estimation of the Photothermal Conversion Efficiency

The photothermal conversion efficiency is an essential property that determines the effectiveness of heat transfer from heated NPs to the surrounding matter (in our case water). In fact, it is a measure of how much of the light energy absorbed by an NP ensemble is transferred to the surrounding matter and should be considered on the nanoscale level. The possibility to present the local heating rate by Eq. (4.1.4) with the conversion efficiency coefficient fm reduces the nanoscale level problem to the microscale description, which ignores the nonhomogeneous temperature distribution around single NPs and considers smooth variations of temperature in water describe by the heat equation (4.1.6) with a continuously distributed heat source.

The comparison of the surface hydrosol temperature distributions measured during laser illumination with the similar ones calculated with COMSOL gives a good possibility to estimate the photothermal conversion efficiency fm. The estimation of fm was performed by the same method that was used for the adjustment of h. The objective function for the estimation of fm is described by the equation

$$\Phi(f_m) = \frac{1}{n_r n_h} \sum_{i=1}^{n_r} \sum_{j=1}^{n_h} \left[ R_{\exp}(r_i, t_j) - R_{cal}(r_i, t_j, f_m) \right]^2 . \qquad (4.3.6)$$

Here Rexp(ri, tj) and Rcal(ri, tj, fm) are the evaluated RTDs and their COMSOL analogues (calculated with h = 1100 W·m-2·K-1 and given fm) at the heating times tj in the annuluses with the external radius and width lpix is the distance corresponding to one pixel on the IR images. nh is the number of heating times considered for the estimation.

The upper left panel of Figure 4.3.4 presents the objective function (4.3.6) calculated for the heat transfer coefficient h = 1100 W·m-2·K-1 and a set of the conversion efficiency coefficient fm ranged from 0.8 to 1. The objective function was calculated for the RTDs measured before heating and after 2, 4, …, 20 s heating (nh = 11) and for a sets of the annuluses with the external radii from 1 to 5 pixels (nr = 5). The objective function exhibit a global minima located at fm = 0.9. This value gives the best match between the measured and calculated RTDs for the points with radii less than 0.1 mm (5 pixels) as it can be seen in the right upper panel of Figure 4.3.3, on which the experimental and calculated with COMSOL RTDs are compared. At higher radii (as in the case of the adjustment of the value h), a noticeable discrepancy between the experimental and calculated RTDs is observed.

The lower left and right panel show the effect of the value fm on the coincidence between the the measured and calculated RTDs. It is possible to see the too small (0.8) or too large (0.9) values lead to the pronounced difference between the experimental and calculated RTDs.

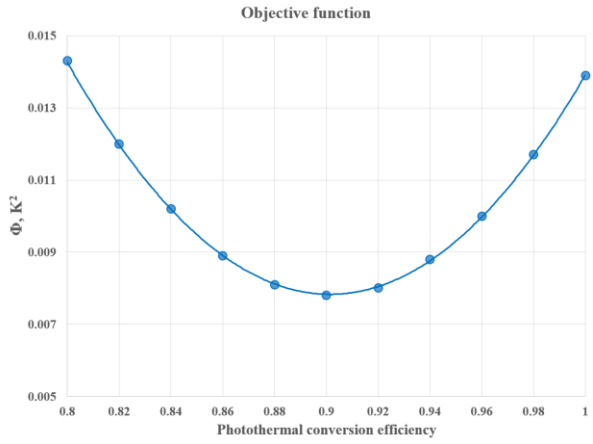


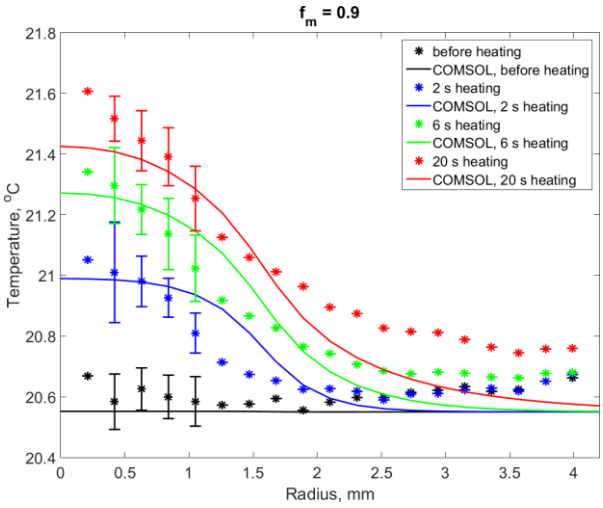

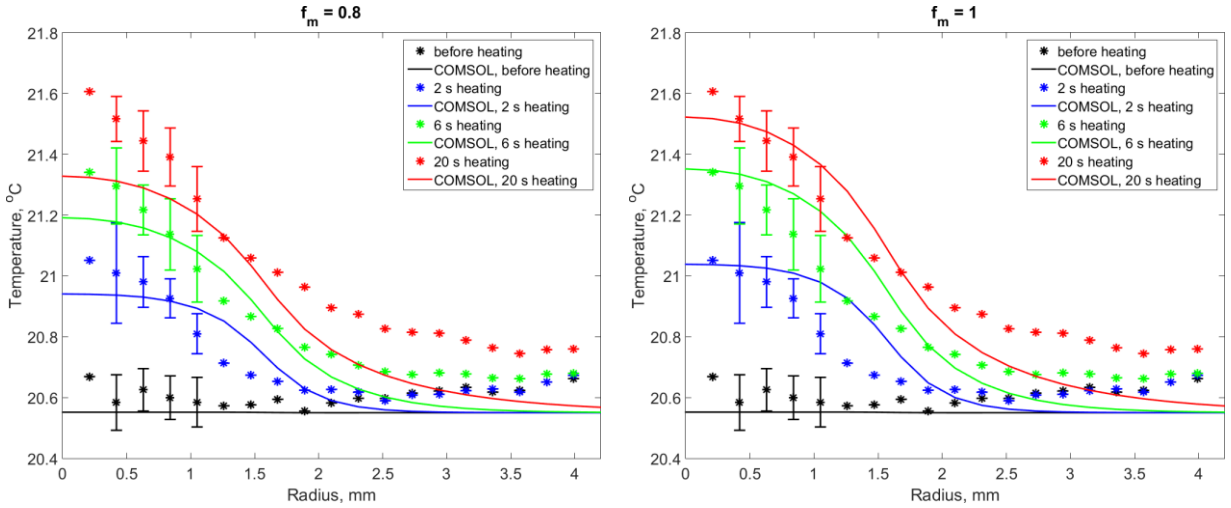


Fig 4.3.3 Upper left: the objective function (4.3.6) as a function of conversion efficiency coefficient fm for the set of the annuluses with the external radii from 1 to 5 pixels (0.21 – 1.05 mm). Upper right, lower left and lower right: comparison of the measured and calculated RTDs for the heating stage. The measured RTDs (points) and their SDs (error bars(*)) are evaluated with the procedure described in the subchapter 3.3.3. The corresponding COMSOL RTDs (lines) are calculated with Eq. 4.3.4 using the surface temperature distribution found with the COMSOL Multiphysics.

(*) The error bars are shown for the points included in the objective function only, the points at r = 0.21 mm that have SD = 0 were also included in the objective function.

## CONCLUSIONS

This works is devoted to develop and implementation of a new improved method for monitoring surface temperature changes by dynamic IR thermography. The method is based on the careful analysis of a set of IR images containing temporal variation of the surface temperature caused by surface or volumetric heating processes due to the external stimulation.

The experimental study on the photothermal effect in a gold hydrosol containing 0.3 mg/mL hollow GNPs with the internal and external radii of about 10 and 13 nm, respectively were performed with a simple experimental set up. The hydrosol surface of 3 mm diameter was illuminated through an optical fiber with laser light (a continuous-wave He-Ne laser, 632.8 nm, 30 mW) delivered falling normally on the hydrosol surface and attenuating by e times at the depth of 1. 7 mm. The surface temperature were measured with a FLIR SC655 InfraRed Camera having the resolution of 640 × 480 pixels. As result, a set of raw IR images of the laser illuminated surface was obtain.

The method based on the careful analysis of a set of raw IR images, which allows one to select areas with significant temperature variation and evaluate temporal behavior of the surface temperature was developed. To realize the method, a set of codes in MATLAB software was written.

The method was applied to the obtained set of raw IR images and spatiotemporal behavior the surface temperature during and after laser illumination were evaluated. It was shown that the surface temperature under the laser beam gradually increases and reaches a saturation level. The surface temperature distribution exhibit the concentric structure with the maximal temperature in the beam center. After the laser was turned off, the temperature returned to equilibrium with the area outside of the beam in about ten seconds.

Numerical simulations of the experiment with the COMSOL Multiphysics Heat Transfer module allowed us reproduce the measured surface temperatures and estimate the heat transfer coefficient at the hydrosol surface and photothermal conversion efficiency (the parameters that would be difficult to find by other methods) as equal to 1100 $W \cdot m^{-2} \cdot K^{-1}$ and 0.9, respectively. The closeness of estimated efficiency to unity evidences that on the microscale the temperature

distribution is more or less homogenous and is determined by a collective heating effect of many GNPs.

In conclusion, this work presents a new improved method for the data acquisition and data analysis based on dynamic IR thermography. This method is not limited to colloids with nanoparticles, but it can be applied for any system whose superficial temperature is change under an external stimulation. Despite the IR тhermography measures only a surface temperature, it is possible, combining the precise surface temperature detection and results of numerical simulations with an adequate model, to estimate the volumetric temperature and determine 3D heat delivery during the hyperthermia procedure.

## REFERENCES


- Akchurin, G.G., Akchurin, G.G., Bogatyrev, V.A., Maksimova, I.L., Seliverstov, G.A., Terentyuk, G.S., Khlebtsov, B.N., Khlebtsov, N.G., Tuchin, V.V., 2007. Near-infrared laser photothermal therapy and photodynamic inactivation of cells by using gold nanoparticles and dyes</title>, in: Dobisz, E.A., Eldada, L.A. (Eds.), . p. 66451U–66451U–12. doi:10.1117/12.733140
- Alam, M., Massoud, Y., 2006. A closed-form analytical model for single nanoshells. IEEE Transactions on Nanotechnology 5, 265–272. doi:10.1109/TNANO.2006.874050
- Avetisyan, A.Y., Yakunin, A.N., Tuchin, V.V., 2010. On the problem of local tissue hyperthermia control: multiscale modelling of pulsed laser radiation action on a medium with embedded nanoparticles. Quantum Electronics 40, 1081–1088. doi:10.1070/QE2010v040n12ABEH014502
- Bäuerle, D.W., 2011. Laser processing and chemistry. Springer Science & Business Media.
- Blackwell, B.F., 1990. Temperature profile in semi-infinite body with exponential source and convective boundary condition. Journal of Heat Transfer 112, 567–571.
- Boyer, D., Tamarat, P., Maali, A., Lounis, B., Orrit, M., 2002. Photothermal imaging of nanometer-sized metal particles among scatterers. Science 297, 1160–1163. doi:10.1126/science.1073765
- Çengel, Y.A., Ghajar, A.J., 2011. Heat and Mass Transfer: Fundamentals and Applications. McGraw-Hill.
- Chiu, M.-J., Chu, L.-K., 2015. Quantifying the photothermal efficiency of gold nanoparticles using tryptophan as an in situ fluorescent thermometer. Physical Chemistry Chemical Physics 17, 17090–17100. https://doi.org/10.1039/c5cp02620b
- Eustis, S., El-Sayed, M.A., 2006. Why gold nanoparticles are more precious than pretty gold: Noble metal surface plasmon resonance and its enhancement of the radiative and nonradiative properties of nanocrystals of different shapes. Chem. Soc. Rev. 35, 209–217. doi:10.1039/B514191E
- Gilchrist R. K., et al. “Selective Inductive Heating of Lymph.” Annals of Surgery 146 (1957) 596-606

- Hirsch,L.R., R. J. Stafford, J. A. Bankson†, S. R. Sershen*, B. Rivera‡, R. E. Price‡, J. D. Hazle†, N. J. Halas§, and J. L. West Nanoshell-mediated near-infrared thermal therapy of tumors under magnetic resonance guidance (2003)
- Hogan, N.J., Urban, A.S., Ayala-Orozco, C., Pimpinelli, A., Nordlander, P., Halas, N.J., 2014. Nanoparticles heat through light localization. Nano Letters 14, 4640–4645. doi:10.1021/nl5016975
- J. V. Sengers and J. T. R. Watson, Improved international formulations for the viscosity and thermal conductivity of water substance, J. Phys. Chem. Ref. Data, 15, 1291, 1986.
- Jain, P.K., Lee, K.S., El-Sayed, I.H., El-Sayed, M.A., 2006. Calculated Absorption and Scattering Properties of Gold Nanoparticles of Different Size, Shape, and Composition: Applications in Biological Imaging and Biomedicine. J. Phys. Chem. B 110, 7238–7248. doi:10.1021/jp057170o
- Jöbsis-vanderVliet, F. Discovery of the near-infrared window into the body and the early development of near-infrared spectroscopy. J. Biomed. Opt. 4, 392-396(1999).
- Khlebtsov, B., Zharov, V., Melnikov, A., Tuchin, V., Khlebtsov, N., 2006. Optical amplification of photothermal therapy with gold nanoparticles and nanoclusters. Nanotechnology 17, 5167. doi:10.1088/0957-4484/17/20/022
- Khlebtsov, N.G., 2008. Optics and biophotonics of nanoparticles with a plasmon resonance. Quantum electronics 38, 504.
- Koziara, J. M. et al. (2003). In Situ Blood-Brain Barrier Transport of Nanoparticles. Pharmaceutical Research Vol. 20, 1772-8
- Kryachko, I.A., Tyutyunnikov, S.I., Shalyapin, V.N., 2010. Calculation of thermal process during the absorption of microwave impulse energy by a spherical nanocluster in liquid medium. Phys. Part. Nuclei Lett. 7, 273–280. doi:10.1134/S1547477110040059
- Lakowicz, J.R., 2006. Plasmonics in Biology and Plasmon-Controlled Fluorescence. Plasmonics 1, 5–33. doi:10.1007/s11468-005-9002-3
- Li, R., Zhang, L., Shi, L., Wang, P., 2017. MXene Ti3C2: An effective 2D light-to-heat conversion material. ACS Nano 11, 3752–3759. doi:10.1021/acsnano.6b08415

- Maksimova, I.L., Akchurin, G.G., Khlebtsov, B.N., Terentyuk, G.S., Akchurin, G.G., Ermolaev, I.A., Skaptsov, A.A., Soboleva, E.P., Khlebtsov, N.G., Tuchin, V.V., 2007. Near-infrared laser photothermal therapy of cancer by using gold nanoparticles: Computer simulations and experiment. Medical Laser Application 22, 199–206. doi:10.1016/j.mla.2007.09.004
- Markolf H. Niemz Laser-Tissue Interactions Fundamentals and Applications Third, Enlarged Edition,2002
- Mishchenko, M.I., Hovenier, J.W., Travis, L.D., 2000. Light scattering by Nonspherical Particles: Theory, Measurements, and Applications
- Mishchenko, M.I., Travis, L.D., Lacis, A.A., 2002. Scattering, absorption, and emission of light by small particles. Cambridge University Press, Cambridge, UK.
- Mishchenko, M.I., Travis, L.D., Lacis, A.A., 2006. Multiple scattering of light by particles: radiative transfer and coherent backscattering. Cambridge University Press, Cambridge, UK.
- Pankhurst, Q. A., et al. (2003). Applications of Magnetic Nanoparticles in Biomedicine. Journal of Physics D: Applied Physics, Vol. 36, pp. R167-81.
- Petriashvili, G., De, S., Chubinidze, K., Hamdi, R., Barberi, R., 2014. Visual micro-thermometers for nanoparticles photo-thermal conversion. Optics Express 22, 14705–14711. https://doi.org/10.1364/OE.22.014705
- Prevo, Shelley A. Esakoff, Alexander Mikhailovsky, Joseph A. Zasadzinski, Scalable Routes to Gold Nanoshells with Tunable Sizes and Response to Near-Infrared Pulsed-Laser Irradiation. Small, Volume 4, Issue 8, Pages 1183–1195).
- Pustovalov, V.K., 2005. Theoretical study of heating of spherical nanoparticle in media by short laser pulses. Chemical Physics 308, 103–108. doi:10.1016/j.chemphys.2004.08.005
- Pustovalov, V.K., 2016. Light-to-heat conversion and heating of single nanoparticles, their assemblies, and the surrounding medium under laser pulses. RSC Adv. 6, 81266–81289. doi:10.1039/C6RA11130K
- Qin, Z., Bischof, J.C., 2012. Thermophysical and biological responses of gold nanoparticle laser heating. Chem. Soc. Rev. 41, 1191–1217. doi:10.1039/C1CS15184C

- Ready, J. F., 1978, Industrial Applications of Lasers, Academic Press, New York.
- Richardson, H.H., Carlson, M.T., Tandler, P.J., Hernandez, P., Govorov, A.O., 2009. Experimental and theoretical studies of light-to-heat conversion and collective heating effects in metal nanoparticle solutions. Nano Lett. 9, 1139–1146. doi:10.1021/nl8036905
- Roper, D.K., Ahn, W., Hoepfner, M., 2007. Microscale heat transfer transduced by surface plasmon resonant gold nanoparticles. Journal of Physical Chemistry C 111, 3636–3641. doi:10.1021/jp064341w
- Sassaroli, E., Li, K.C.P., O'Neill, B.E., 2009. Numerical investigation of heating of a gold nanoparticle and the surrounding microenvironment by nanosecond laser pulses for nanomedicine applications. Physics in Medicine and Biology 54, 5541–5560. doi:10.1088/0031-9155/54/18/013
- Sato, F., Malacarne, L.C., Pedreira, P.R.B., Belancon, M.P., Mendes, R.S., Baesso, M.L., Astrath, N.G.C., Shen, J., 2008. Time-resolved thermal mirror method: A theoretical study. Journal of Applied Physics 104. doi:10.1063/1.2975997
- Shao Hsuan Tsao,† Dehui Wan,*,† Yu-Sheng Lai,‡ Ho-Ming Chang,‡ Chen-Chieh Yu,§ Keng-Te Lin,§ and Hsuen-Li Chen§ White-Light-Induced Collective Heating of Gold Nanocomposite/ Bombyx mori Silk Thin Films with Ultrahigh Broadband Absorbance. (2015)
- Shuichi Hashimotoa, Daniel Werner a, Takayuki Uwada ;Studies on the interaction of pulsed lasers with plasmonic gold nanoparticles toward light manipulation, heat management, and nanofabrication ;2012
- Takami, A., Kurita, H., Koda, S., 1999. Laser-induced size reduction of noble metal particles. The Journal of Physical Chemistry B 103, 1226–1232.
- Terentyuk, G.S., Maslyakova, G.N., Suleymanova, L.V., Khlebtsov, N.G., Khlebtsov, B.N., Akchurin, G.G., Maksimova, I.L., Tuchin, V.V., 2009. Laser-induced tissue hyperthermia mediated by gold nanoparticles: toward cancer phototherapy. Journal of Biomedical Optics 14, 21016. doi:10.1117/1.3122371
- Wang, L., Zhou, X., Wei, X., 2008. Heat Conduction: Mathematical Models and Analytical Solutions. Springer Science & Business Media.

- Weissleder, R. A clearer vision for in vivo imaging. Nat. Biotechnol. 19, 316-317 (2001).
- Welch, A.J. & van Gemert, M.J.C. (eds.) Optical-Thermal Response of Laser; American Surgical Association, Chicago, Illinois, May 8-10,
- Yilbas, B.S., Shuja, S.Z., 2013. Laser Surface Processing and Model Studies, Materials Forming, Machining and Tribology. Springer Berlin Heidelberg, Berlin, Heidelberg. doi:10.1007/978-3-642-36629-1
- Zhenpeng Qin , Laser Induced Gold Nanoparticle Heating: Thermal Contrast in Lateral Flow Immunoassays, June, 2014